eScience xxx (xxxx) xxx

Contents lists available at ScienceDirect

eScience

journal homepage: www.keaipublishing.com/en/journals/escience

Review

Electronic structure regulation of noble metal-free materials toward alkaline oxygen electrocatalysis

Xia Wang [a], Minghao Yu [b,*], Xinliang Feng [b,c,*]

[a] Max-Planck-Institute for Chemical Physics of Solids, 01187 Dresden, Germany
[b] Centre for Advancing Electronics Dresden (CFAED) & Faculty of Chemistry and Food Chemistry, Technische Universität Dresden, 01062 Dresden, Germany
[c] Max Planck Institute of Microstructure Physics, 06120 Halle, Germany

HIGHLIGHTS

- The relationship between electronic structure and catalytic activity is analyzed.
- Diverse electronic structure regulation strategies are summarized.
- Future perspectives on designing advanced oxygen electrocatalysts are offered.

GRAPHICAL ABSTRACT

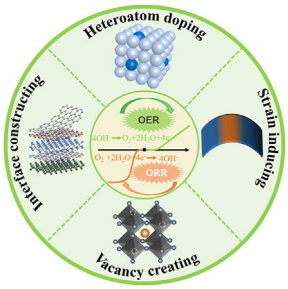

ARTICLE INFO

Keywords:
Oxygen electrocatalysts
Electronic structure
Noble metal-free electrocatalysts
Active sites
Intrinsic activity

ABSTRACT

Developing highly efficient, inexpensive catalysts for oxygen electrocatalysis in alkaline electrolytes (i.e., the oxygen reduction reaction (ORR) and the oxygen evolution reaction (OER)) is essential for constructing advanced energy conversion techniques (such as electrolyzers, fuel cells, and metal–air batteries). Recent achievements in efficient noble metal-free ORR and OER catalysts make the replacement of conventional noble metal counterparts a realistic possibility. In particular, various electronic structure regulation strategies have been employed to endow these oxygen catalysts with attractive physicochemical properties and strong synergistic effects, providing significant fundamental understanding to advance in this direction. This review article summarizes recently developed electronic structure regulation strategies for three types of noble metal-free oxygen catalysts: transition metal compounds, single-atom catalysts, and metal-free catalysts. We begin by briefly presenting the basic ORR and OER reaction mechanisms, following this with an analysis of the fundamental relationship between electronic structure and intrinsic electrocatalytic activity for the three categories of catalysts. Subsequently, recent advances in electronic structure regulation strategies for noble metal-free ORR and OER catalysts are systematically discussed. We conclude by summarizing the remaining challenges and presenting our outlook on the future for designing and synthesizing noble metal-free oxygen electrocatalysts.

1. Introduction

The electrocatalytic oxygen reduction reaction (ORR) and oxygen evolution reaction (OER) in alkaline electrolytes are two significant heterogeneous reactions for sustainable energy conversion technologies, including electrolyzers, metal–air batteries, and fuel cells [1,2]. However, as both oxygen reactions involve multiple intermediates and multi-electron processes, they undergo large overpotentials and sluggish

* Corresponding authors.
E-mail addresses: minghao.yu@tu-dresden.de (M. Yu), xinliang.feng@tu-dresden.de (X. Feng).

https://doi.org/10.1016/j.esci.2023.100141
Received 29 November 2022; Received in revised form 9 February 2023; Accepted 9 May 2023
Available online xxxx

Please cite this article as: X. Wang et al., Electronic structure regulation of noble metal-free materials toward alkaline oxygen electrocatalysis, eScience, https://doi.org/10.1016/j.esci.2023.100141

kinetics [3]. Consequently, the corresponding energy conversion devices deliver large voltage polarization, resulting in inferior energy efficiency or low output power. As a vital part of such energy conversion devices, oxygen electrocatalysts play a key role in addressing these issues. Many compounds based on first- and second-row transition metals suffer from instability in acidic media during the ORR and OER, and thus their applications in energy devices with acidic electrolytes are limited [4]. In contrast, the ORR and OER in alkaline conditions are kinetically favored and show less susceptibility to corrosion, enabling the stable use of less-expensive materials [5,6]. Today, Pt-based materials are well known as benchmark ORR catalysts in commercialization, while Ir-/Ru-based catalysts are prominent for the OER. These noble metal-based catalysts generally suffer from high cost, low crustal abundance, and inferior durability [7]. Therefore, tremendous efforts have been made in recent decades to search for cost-effective noble metal-free electrocatalysts as alternatives.

Strategies used to improve the catalytic activity of noble metal-free electrocatalysts can be roughly divided into two categories, namely enhancing the intrinsic activity of the single site and improving the active site density. The latter can be easily achieved by controlling the catalyst morphology and porosity at the micro or nano level. By contrast, to regulate the intrinsic activity of a single active site, structural engineering of the catalyst must occur at the atomic level, which requires highly precise structural control over the catalytic sites. On the basis of the classic Sabatier principle, efficient catalysts bind reaction intermediates with optimal strength, meaning neither too weak to activate the intermediates nor too strong to facilitate reactant desorption [8]. To this end, several electronic structure parameters (e.g., d-band position, e_g filling, density of state (DOS), spin ordering) have been extracted as important descriptors to evaluate the "bonding strength" between reactants and active sites [9]. Accordingly, various electronic structure engineering strategies, such as heteroatom doping, vacancy creation, strain induction, and interface construction, have been proposed to optimize the intrinsic activity of the single catalytic site. Moreover, the fundamental understanding acquired from electronic structure engineering provides opportunities for advanced modelling techniques, such as high-throughput DFT calculations, artificial intelligence, and machine learning. By employing the electronic structure descriptors discussed above [10], these advanced modelling tools are of significance in establishing universal structure–catalytic performance relationships, predicting the performance of new catalysts, and thus accelerating the rational design of promising catalysts by bypassing time-consuming trials.

To date, several excellent review articles have provided intensive discussions on oxygen electrocatalysts with respect to the catalyst structures developed to date, important descriptors for catalytic activity, and applications in energy conversion devices [11–14]. To differentiate it from the previous review efforts, this article particularly focuses on the electronic structure regulation strategies employed to improve the intrinsic activity for three types of noble metal-free oxygen catalysts (i.e., transition metal compounds, single-atom catalysts (SACs), and metal-free catalysts) in alkaline electrolytes (Fig. 1). We begin by introducing ORR and OER mechanisms. Then, the fundamental principles underlying different electronic structure regulation strategies are comprehensively analyzed. These strategies are categorized into heteroatom doping, vacancy creation, strain induction, and interface construction. Afterwards, we discuss recently developed strategies for engineering electronic structures in the three categories of noble metal-free catalysts. Finally, we highlight the critical challenges in designing advanced oxygen electrocatalysts for alkaline environments and offer our perspectives on possible future efforts in this field.

2. ORR and OER fundamentals

2.1. ORR mechanism

Two reaction pathways for the ORR in alkaline electrolyte have been identified. One is the four-electron ($4e^-$) path to produce OH^-, while the other is the two-electron ($2e^-$) process to generate hydrogen peroxide (H_2O_2).

The ORR pathway primarily relies on the nature of the catalyst [18]. For example, two O_2 adsorption configurations occur on the active sites,

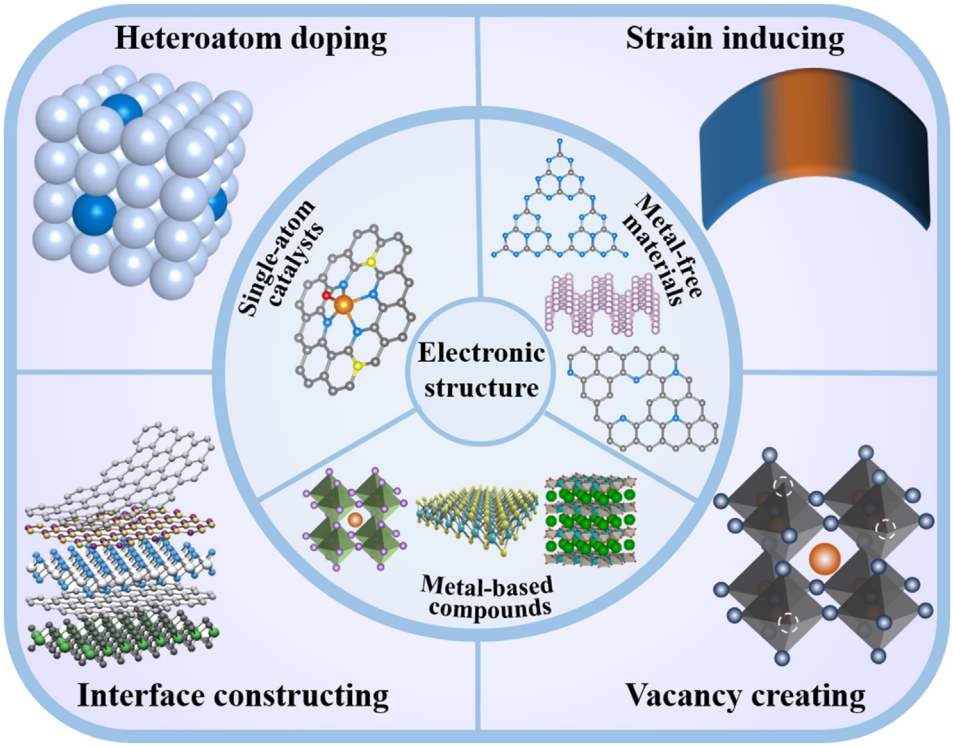

Fig. 1. Schematic illustration showing the electronic structure regulation strategies for different noble metal-free electrocatalysts.

namely, the side-on configurations (Fig. 2a, I-II) and the end-on configurations (Fig. 2a, III-IV) [19]. With two "in-parallel" O atoms coordinated with active sites, the side-on O_2 adsorption configurations favor O_2 dissociation, thus likely leading to the direct $4e^-$ pathway. Meanwhile, the end-on configurations, with only a single O atom "perpendicularly" coordinated to the active site, favor the indirect $2e^-$ transfer pathway. The peroxide species formed during the $2e^-$ process are corrosive and lower the stability of the corresponding metal–air batteries and fuel cells, making the $4e^-$ pathway preferable to generate high output power density for these devices [20,21]. Therefore, this review particularly discusses the associative mechanism for the $4e^-$ ORR pathway in alkaline environments.

In the $4e^-$ ORR pathway, different oxygen intermediates — i.e., OOH*, O*, and OH* — are adsorbed sequentially on the active sites. Based on density functional theory (DFT) calculations, Nørskov *et al.* found the scaling relationship between adsorption energies for OOH* (ΔG_{OOH^*}) and OH*(ΔG_{OH^*}): $\Delta G_{OOH^*} = \Delta G_{OH^*} + 3.2 \pm 0.2$ eV [22,23]. The reactivity of each step relies heavily on the oxygen intermediate adsorption properties on the catalytic active site. For example, for metal-based catalysts that bind OH* strongly, the last step, i.e., equation (5) ($OH^* \rightarrow OH^-$), is the rate-determining step (RDS), whereas the O_2 activation in the first step, i.e., equation (2) ($O_2 \rightarrow OOH^*$), is the RDS for active metal sites possessing weak bonding strength for O_2. The correlation between intermediates' adsorption energies and ORR activities can be described by volcano plots (Fig. 2b) [15]. This criterion applies not only to metal catalysts but also to the emerging SACs. Moreover, the peak position of the volcano plot is usually occupied by Pt-based catalysts, while Fe-based SACs are close to the optimum ORR activity, presenting potential alternatives for Pt-based catalysts. Guided by the volcano plots, one needs to finely tune the electronic structure of the active site to optimize the adsorption strength for the oxygen intermediates in order to improve the catalysts' intrinsic activity.

Among all the electronic structure descriptors for ORR (e.g., e_g filling, d-band theory, p-band center of O, charge-transfer energy, Fermi softness, as well as average O *2p* state energy) [13], e_g filling and d-band theory are the most prevalent for predicting the activities of ORR catalysts. For example, e_g filling at octahedral sites was successfully used to analyze the catalytic behavior of transition-metal oxides (spinels, perovskites) [16]. Specifically, one principle to improve the intrinsic ORR activity of perovskites is to enable e_g filling to be close to 1 (Fig. 2c). This was investigated by employing a series of perovskite oxides as ORR catalysts. A combination of characterization techniques can be used to experimentally determine e_g fillings, such as X-ray absorption (XAS) [16], X-ray emission spectroscopy [24], thermogravimetric analysis (TGA) [25], and magnetic measurement [25]. The RDS of the ORR is affected by the energy obtained from delivering a single σ*-antibonding e_g electron via the competitive displacement of a rate-limiting O_2^{2-}/OH^- exchange, and surficial OH^- regeneration.

Nørskov developed d-band theory [26]. When oxygen intermediates react on active sites, the localized d-band center dominates the bonding strengths between the adsorption species and active sites. Thus, the volcano relationship of the d-band center is related to the Fermi level (E_f), and the ORR activity is established. Generally, in metal-based catalysts, the OH* and O* adsorption energies vary linearly with the d-band center of the metal active sites. A higher d-state energy for a metal indicates a more negative ΔG_{OH^*} and higher catalyst reactivity. Pt, which has an appropriate d-band center position, is so far considered the single metallic ORR electrocatalyst with the highest efficiency. However, ORR

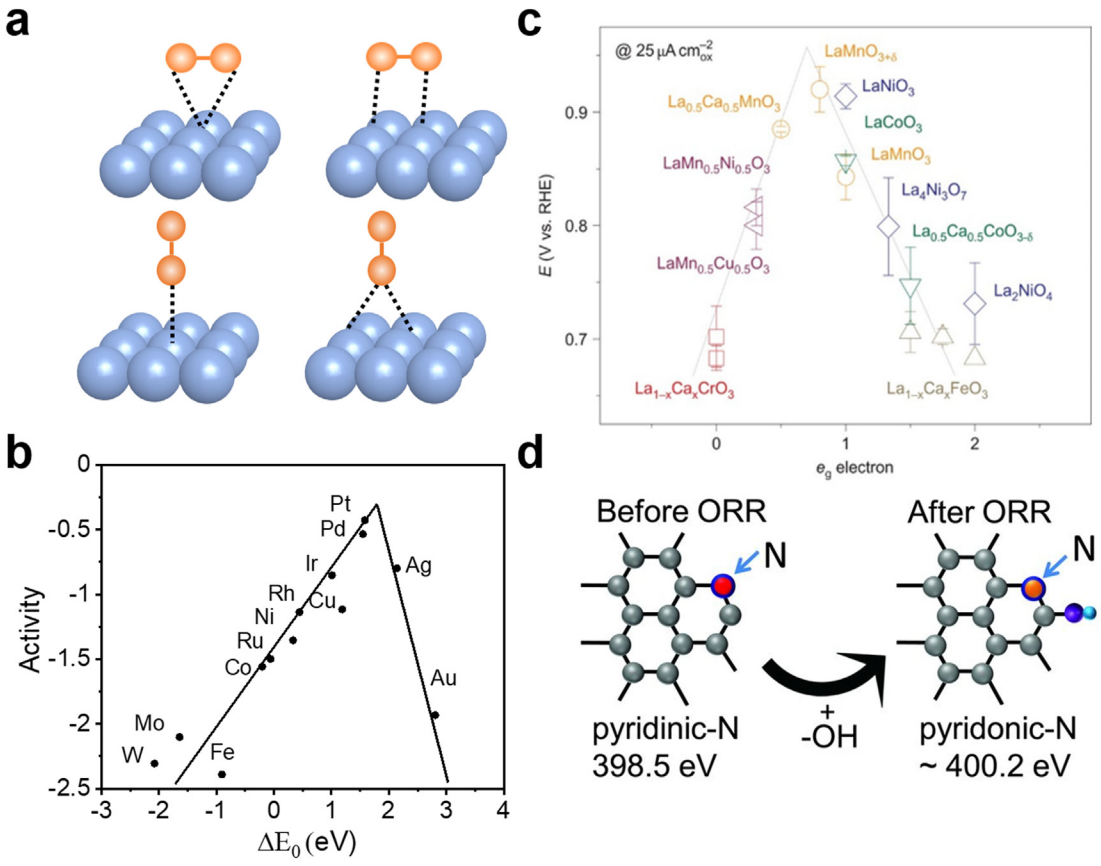

Fig. 2. Illustration of different oxygen adsorbate configurations: (I) the on-top side-on, (II) the bridge side-on, (III) the on-top end-on, and (IV) the bridge end-on. (b) ORR activity as a function of the oxygen binding energy. Reproduced with permission [15]. Copyright 2004, American Chemical Society. (c) ORR activity of perovskite oxides. Reproduced with permission [16]. Copyright 2011, Nature Publishing Group. (d) Schematic images illustrating the pyridinic N formation originating from OH attachment to the C atom next to pyridinic N. Reproduced with permission [17]. Copyright 2016, American Association for the Advancement of Science.

electrocatalysts possessing metal–oxygen bond strength 0.0–0.4 eV weaker than that of Pt can further enhance the activity [27]. Therefore, strategies such as heteroatom doping, vacancy creation, strain induction, and interface construction could push the ORR activity toward the volcano peak by adjusting the metal–oxygen bonding and optimizing the d-band center [11].

As for metal-free catalysts based on carbon materials, heteroatom doping into the carbon framework can efficiently modulate the electronic structure of the surrounding C atoms and simultaneously modify the local charge density distribution, thus promoting the ORR activity [28]. For instance, Nakamura et al. assigned the active sites and reaction pathways for the ORR using a N-doped pyrolytic highly oriented graphite model catalyst [17]. They clarified that the carbon atoms next to the pyridinic N were ORR active sites in N-doped carbon materials (Fig. 2d). Besides heteroatom doping, topological defects and edge sites also play significant roles in tuning the charge distribution of carbon-based metal-free materials and thereby regulating the catalytic performance [29].

2.2. OER mechanism

It remains challenging to determine the details of OER pathways. The widely accepted OER mechanisms in alkaline electrolytes include two possible pathways: the adsorbate evolution mechanism (AEM) and the lattice-oxygen-mediated mechanism (LOM) (Figs. 3a and b) [30].

In the conventional AEM process, OER occurs on a single active site (e.g., transition metal atom). The corresponding elementary steps can be described as the reverse of the ORR process. Similar to the ORR, the binding energy of OER intermediates (OH* and OOH*) follows the scaling relationship [1]. Consequently, the minimum overpotential (η) of a catalyst relies on the O* energy level between that of OH* and OOH*, which means that these steps will be the RDS [31]. The overpotential of the OER can be expressed by equation (1). Therefore, volcano plots of the OER can be established for various metal oxide surfaces (perovskites, rutile, rock salts, spinel, and bixbyite oxides, etc.) using $\Delta G_{O^*} - \Delta G_{OH^*}$ (Fig. 3c and d) [31]. For the catalysts appearing on the left side of the volcano plots, the RDS is the generation of OOH*, whereas for the weak oxygen-bonding branch on the right side of the volcano plots, the deprotonation of OH* is the RDS.

$$\eta = \max[(\Delta G_{O^*} - \Delta G_{OH^*}), (\Delta G_{OOH^*} - \Delta G_{O^*})]/e - 1.23\ V = \max[(\Delta G_{O^*} - \Delta G_{OH^*}), 3.2\ eV - (\Delta G_{O^*} - \Delta G_{OH^*})]/e - 1.23\ V \quad (1)$$

With OER volcano plots, one can expect to get an excellent electrocatalyst with an optimized $\Delta G_{O^*} - \Delta G_{OH^*}$ value via regulating the electronic structure. The electronic structure corresponding to the binding energy of the OER intermediates on the active sites can be applied to describe the structure–activity relationship of catalysts. Among all the electronic structure descriptors for the OER, e_g filling and metal–oxygen covalency are the most widely used [34].

In e_g filling theory, the bonding strength with oxygen intermediates is associated with e_g orbital occupancy, i.e., a higher e_g occupancy implies weaker bonding with intermediates, and vice versa. Based on this principle, Shao-Horn *et al.* systematically investigated the e_g occupancy in perovskites and found that the e_g occupancy of the *3d* electron could be a descriptor for the activity [32]. They predicted that optimal perovskites for the OER would have an e_g occupancy value close to 1 (Fig. 3e). Calculation of e_g occupancy was achieved by using XAS to estimate the oxidation state of the active site and TGA to quantify the oxygen vacancy degree. Yet despite the success of the molecular orbital concept and the establishment of e_g filling theory, it remains difficult to determine the e_g occupancy in some cases [10]. Moreover, the e_g filling theory fails to explain why some perovskites (i.e., $LaMnO_3$, $LaCoO_3$, and $LaNiO_3$) possess the same e_g occupancy ($e_g = 1$) but exhibit different activities [32]. The underlying reason is that the e_g orbital occupancy is estimated for the metal atom using the ionic model, which cannot capture the sharing of electrons along the metal–oxygen bond. In this regard, Shao-Horn et al. revealed that better OER performance could be achieved by enhancing covalent mixing (denoted as $hole_{eg} + 1/4\ hole_{t_{2g}}$) between the B site octahedral coordinated metal cations and O anions with an e_g filling of 1 [32]. O *K*-edge XAS spectra were collected to estimate the metal–oxygen covalency. Specifically, the normalized O XAS spectra

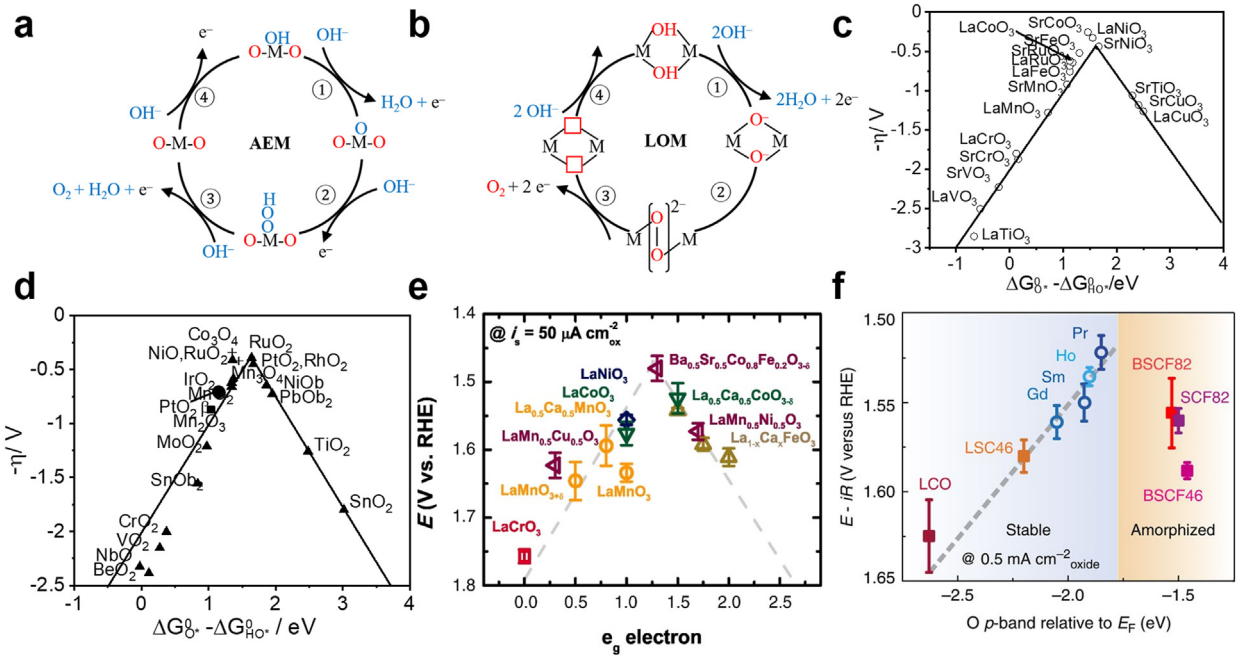

Fig. 3. Schematic of the (a) AEM and (b) LOM OER mechanisms. Reproduced with permission [30]. Copyright 2016, Nature Publishing Group. OER activity volcano plots for (c) perovskite oxides and (d) rutile, anatase, Co_3O_4, Mn_xO_y oxides, with the bonding strength of $\Delta G_{O^*} - \Delta G_{OH^*}$ as the activity descriptor. Reproduced with permission [31]. Copyright 2011, Wiley-VCH. (e) Relationship between OER activity and e_g occupancy for transition metals. Reproduced with permission [32]. Copyright 2011, American Association for the Advancement of Science. (f) Relationship between OER activity and oxygen p-band center in double perovskites. The inset shows a schematic of the O p-band of transition metal oxides. Reproduced with permission [33]. Copyright 2013, Nature Publishing Group.

reflected electron excitation from O *1s* to B *3d* - O *2p*. The spectra probed the u symmetry portion of the unoccupied state, which is intrinsic to the *2p* orbital of the O atom. Absorbance is related to the unoccupied *2p* orbital ("ligand hole"). By using the dipole operator approximation, the metal–oxygen hybridization was quantified [16]. A higher metal–oxygen covalency implied the B-site cation at the active redox couple had a larger O *2p* character, which improved charge transfer between the adsorbates during the RDS for the OER and active sites (Fig. 3f). Furthermore, shifting the O p-band center closer to the E_f increased the OER activity, while having the O p-band center too close to E_f decreased the stability of oxides in the OER. Double and pseudo-cubic perovskite oxides whose O p-band center is very near the E_f should show the highest OER activity in an alkaline solution [33].

In the LOM mechanism, the lattice oxygen from the catalyst takes part in the reaction (Fig. 3b). Specifically, two OH* first adsorb at the dual metal active sites and then deprotonate to obtain two metal-oxo intermediates. Subsequently, the two-neighboring metal-oxo intermediates bind directly to generate an O–O bond rather than OOH*. Next, O_2 is released via coupling with the lattice oxygen and forming an oxygen vacancy in the catalyst lattice. Finally, the two vacant metal centers are refilled by OH^- in the electrolyte [35]. Since the LOM process bypasses the generation of OOH*, the scaling relationship between OOH* and OH* is no longer applicable. Indeed, in many metal oxide catalysts, the LOM process presents higher OER performance than the traditional AEM process. For example, Shao et al. distinguished the contribution of lattice oxygen participation in the OER process by the LOM mechanism in Si-doped strontium cobaltite perovskites (Si–SCO) [36]. The Si–SCO exhibited a 12.8-fold improvement in oxygen diffusivity, which was well matched with the 10-fold enhancement of its intrinsic OER activity compared to pristine SCO. Although the OER through the AEM and LOM mechanisms occurs simultaneously, the boosted electrocatalytic activity via Si doping is predominantly due to the participation of lattice oxygen in the LOM.

How the LOM competes with the AEM in the OER remains elusive. It has been proven that with increased metal–oxygen covalency, the OER mechanism will switch from the AEM to the LOM [10,30]. For instance, when the metal d-band position is above the O p band, the metal center serves as the redox center, enabling the OER process to follow the AEM. Conversely, when the occupied metal d-band has a lower energy level compared with the O p-band, electrons transfer from the O p-band to the metal d-band, producing ligand holes. The ligand holes facilitate the generation of oxygenated $(O_2)^{n-}$ species by structural arrangement, reducing energy to reach a stable state. This observation implies that the OER redox center should provide or accept electrons with energy close to the thermodynamic potential of oxygen in water, i.e., 1.23 V vs. the reversible hydrogen electrode (RHE). Eventually, when the metal–oxygen covalency is enlarged, the OER mechanism generally switches from AEM to LOM.

3. Noble metal-free catalysts

3.1. Transition metal compounds

Non-noble transition metal compounds (including transition metal oxides, carbides, nitrides, phosphides, (oxy)hydroxides, and chalcogenides) are an important category of ORR and OER catalysts. In transition metal compound materials, crystalline nature, crystal plane, and composition all play an important part in the intrinsic catalytic activity. In this section, we will analyze the crystal structure of different transition metal compounds and the relationship correlating their electronic structures to their intrinsic ORR/OER activities.

3.1.1. Transition metal oxides

Oxygen electrocatalysts based on transition metal oxides (TMOs) feature high abundance, low price, environmental friendliness, desirable activity, as well as sufficient stability under alkaline conditions. Amongst them, perovskite oxides are especially attractive due to their high composition flexibility and tunable electronic structures. Advanced perovskite catalysts show ORR catalytic activity comparable to or even higher than noble metal-based electrocatalysts. They have a general formula of ABO_3, where A is an alkaline- or rare-earth element (e.g., Ba, La, Pr, Sr, Ca), while B is a transition metal (e.g., Ni, Co, Fe, Mn, Cr, Cu) [37]. A perfect cubic perovskite structure is assigned to space group *Pm3m-Oh 1*, where the B site has 6-fold and the A site has 12-fold coordination with O anions (Fig. 4a). The substitution of A and/or B sites confers high flexibility for modifying the electronic structure, thus providing huge room to tune their catalytic properties. Moreover, the numerous substitutions possible at both A and B sites also lead to ready control over the metal valence states, together with the generation of oxygen vacancies, making perovskites a good material library for understanding the structure–catalytic property relationship [38].

Spinel oxides are another group of TMO-based catalysts, represented by the formula $A_xB_{3-x}O_4$ (where A is a divalent transition metal ion, e.g., Zn^{2+}, Cu^{2+}, Mg^{2+}, Fe^{2+}, Ni^{2+}, Co^{2+}, Mn^{2+}; and B is a trivalent metal ion, e.g., Al^{3+}, Fe^{3+}, Co^{3+}, Cr^{3+}, Mn^{3+}). The presence of multivalent cations provides donor–acceptor chemisorption positions that can adsorb oxygen reversibly, giving spinel oxides activity for both the ORR and the OER. In spinel oxides, the two tetrahedral and octahedral metal sites are respectively occupied by A and B cations with different atom ratios (Fig. 4b) [42]. The e_g orbitals of octahedrally coordinated metal cations point directly to intermediates, thus giving rise to strong spatial overlap with O *2p* orbitals and leading to high chemical interaction with oxygen species. In this sense, the metal ions in octahedral sites have been widely considered as active sites in spinel oxides. The ORR/OER performance of spinel oxides greatly depends on the diverse electronic structure of octahedrally coordinated metal cations, e.g., e_g filling, spin state, and metal–oxygen bond covalency [43]. Engineering the electronic structure of spinel oxides can be done by heteroatom doping, creating lattice defects, and tuning relative ions in the composition to obtain desirable active sites [44]. Coupling with various substrates and inducing strain are also efficient strategies to modify the electronic structures of spinel oxides, thus adjusting their ORR and OER activities [45].

3.1.2. Transition metal carbides and nitrides

Generally, transition metal carbides (TMCs) and transition metal nitrides (TMNs) are made up of metal elements from groups IVB to VIIIB and can have several formulas, such as MC/MN, M_2C/M_2N, M_3C, and M_4N [46]. They show the same crystal structure as their parent metals, as the small C/N atoms are prone to locate at the interstitial sites in their parent metal lattices. TMCs and TMNs feature close-packed hexagonal, face-centered cubic (fcc), or simple hexagonal structures. For example, monocarbides/nitrides (e.g., TiC/TiN, ZrC/ZrN, and TaC/TaN) usually display a fcc structure, while M_2C/M_2N, M_3C, and M_4N possess complicated atomic arrangements with hexagonal and orthorhombic structures. The electronic structure of TMCs and TMNs can be modified by doping C and N into the metal lattice, which in turn alters the surface chemical properties of TMCs and TMNs. Moreover, the doping of C/N atoms expands the parental lattice, resulting in a contraction of the metal d-band and causing enhanced DOS near E_f. The DOS redistribution is believed to induce comparable catalytic properties to noble metal-based catalysts [47]. Consequently, metallic TMCs/TMNs not only demonstrate the good electronic conductivity of the parent metals but also deliver comparable electrocatalytic performance as noble metal-based catalysts [48].

Recently, emerging two-dimensional (2D) TMCs/TMNs, so-called "MXenes", have been intensively investigated and applied in energy conversion applications. MXenes possess close-packed hexagonal structures featuring *$P6_3/mmc$* group symmetry, in which the M sites (transition metal atoms like Ti, Nb, Mo, V, and W) are close-packed in a 2D honeycomb-like lattice, while the X atoms (C and/or N) take up the octahedral positions in between M atomic planes [49]. MXenes follow a general formula of $M_{n+1}X_nT_x$ (n = 1–3) (e.g., Ti_2CT_x [50], $Ti_3C_2T_x$ [49], and $Nb_4C_3T_x$ [51]), where T_x are the surface terminations (e.g., –O, –F,

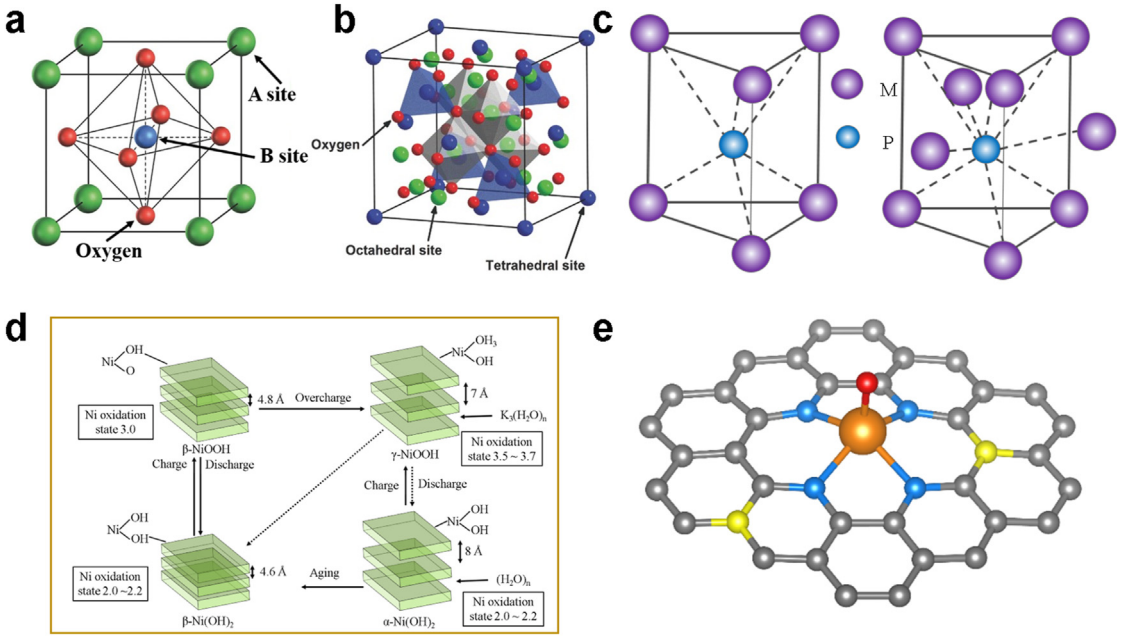

Fig. 4. (a) Schematic of an ideal perovskite oxide unit cell, where A is a rare- or alkaline-earth metal element, while B is a transition metal. Reproduced with permission [16]. Copyright 2011, Nature Publishing Group. (b) Schematic for the spinel crystal structure. Reproduced with permission [39]. Copyright 2011, Wiley-VCH. (c) Triangular prism (left) and tetrakaidekahedral (right) structures in phosphides. (d) Schematic of Bode's diagram of the Ni (II)/Ni (III) redox transition in Ni hydroxide layers. Reproduced with permission [40,41]. Copyright 2013, Royal Society of Chemistry. (e) Geometric structure for SACs, where orange spheres, blue spheres, yellow spheres, red spheres, and grey spheres represent the center metal atoms, local coordination atoms, environmental atoms, guest groups, and carbon atoms, respectively.

and –OH functional groups) [52]. The interplay of M with C, N, and surface terminations modulates the electronic structure of MXenes, making them promising candidates for oxygen electrocatalysis [53]. However, the utilization of MXenes as ORR and OER electrocatalysts is still in its infancy. Extended research on diverse MXenes is expected to confirm their suitability as a novel group of efficient and affordable ORR and OER electrocatalysts.

3.1.3. *Transition metal phosphides*

Transition metal phosphides (TMPs) have many merits, such as good electronic conductivity, abundance, as well as excellent physicochemical properties, thus generating substantial interest as oxygen electrocatalysts. Unlike TMCs/TMNs with interstitial structures, TMPs normally have P atoms positioned at a triangular prism center consisting of transition metal atoms, because P is 1.5 times larger in diameter (0.109 nm) than C (0.065 nm) and N (0.071 nm) (Fig. 4c, left) [54]. In metal-rich compositions, the nearest neighbors number rises to form a 9-fold tetrakaidekahedral structure with more metal atoms positioned near the vertical face centers of the prism. Such a structure offers good accessibility to the edge sites and active corners of the TMPs' surfaces (Fig. 4c right) [55].

TMPs can be considered phosphorus–metal “alloys.” It has been revealed that the E_f and d-band center of a metal can be shifted after the introduction of P atoms, resulting in different catalytic activities [56]. Therefore, the good catalytic activity of TMPs is possibly because they have distinct electronic structures caused by the presence of P. Two methods have been utilized to modify the intrinsic activity of TMPs: tuning the stoichiometric P/M ratio and elemental alloying/doping. For example, Qiu et al. controlled the Ni/Co ratio in Ni–Co phosphide nanocages. It was suggested that an appropriate Co doping concentration increased the DOS at the E_f and shifted the metal d-states close to the E_f, enabling higher charge carrier density and lower adsorption energy for intermediates compared with Ni_2P and CoP [57]. Therefore, the as-developed Ni–Co bimetal phosphide nanocages showed considerably better OER activity than Ni_2P and CoP.

3.1.4. *Transition metal (oxy)hydroxides*

First-row transition metal (oxy)hydroxides (particularly Ni- or Co-containing 2D layered double hydroxides (LDH)) are the earliest-identified OER catalysts and have been a hot subject for the past decade [58]. Taking $Ni(OH)_2$ as an example, the surface structure during the OER in an alkaline solution evolves according to Equation (15), where Ni^{2+} from $Ni(OH)_2$ is oxidized into Ni^{3+} in NiOOH. The specific phase transformation is illustrated in Bode's diagram (Fig. 4d) and includes four phases [40,41]. All four consist of Ni metal centered edge-sharing octahedral layers as well as O/OH groups at vertices, pointing at both layer sides along the stacking direction (i.e., c-axis). Specifically, the α-$Ni(OH)_2$ phase (Ni oxidation state of ~2) exhibits a disordered phase, while the γ-NiOOH phase (Ni oxidation state of 3.5–3.7) can incorporate charge-balancing cations between layers. The β-$Ni(OH)_2$ (Ni oxidation state of ~2) and β-NiOOH phases (Ni oxidation state of ~3) are not hydrated and do not accommodate ions between layers. The layer distance changes significantly among the four phases. Besides these four, other crystal structures with various interlayer distances have also been regarded as interstratified mixed α- and β-phases, in which partial water intercalation leads to the variable interlayer distance [59].

$$Ni(OH)_2 + OH^- \rightarrow NiOOH + H_2O + e^- \quad (15)$$

The OER activity can be substantially improved by incorporating Fe into NiOOH. For instance, when the Fe content reached 25%, the OER overpotential of $Ni_{1-x}Fe_xOOH$ was decreased by 0.2 V [60]. Fe ions tend to be doped on the edge, surface, or defect sites of NiOOH, influencing the Ni redox behavior to a remarkable extent. But controversial statements have been made about the real active site in Fe-incorporated NiOOH. One view states that Fe species act as the main catalytic centers, while the other claims that the improved activity of Ni sites originates from the electronic structure regulation induced by Fe incorporation. Recently, Dionigi *et al.* proposed that Fe-M sites (M = Ni or Co) surpassed both M-M sites and Fe sites by stabilizing OER intermediates via an O-bridged configuration [61].

Similar to TMOs, various electronic structure regulation strategies have been proposed for metal (oxy)hydroxide catalysts, including cationic/anionic regulation, defect engineering, and surface modification [62]. For example, Sargent *et al.* reported a room-temperature synthetic method to develop gelled Fe–Co–W oxyhydroxides [63]. DFT suggested that non-*3d* high-valence W doping modulated pristine Fe–Co oxyhydroxides generated near-ideal OER intermediate adsorption energies. Among all the pure phases, gelled Fe–Co–W oxyhydroxides exhibited the lowest $E_{j\,=\,10}$ (1.421 V) in 1 M KOH electrolyte. In addition, Zhang et al. demonstrated an anionic regulation method to regulate the covalency and ionicity of cation–anion interactions in Ni–Fe (oxy)sulfides and promote their OER performance [64]. The polarized S and non-polarized O synergistically regulated the electronic structure of active metal sites through electronic interaction with Ni and Fe ions. Dispersive electrons from polarized anions were shared with adjacent cations, thus affecting the ionicity and covalency of the cation–anion interaction. Moreover, Wang's group used Ar plasma to etch bulk Co–Fe LDHs and obtained ultrathin LDH nanosheets as an excellent electrocatalyst for the OER [65]. Multiple vacancies (V_o, V_{Co}, and V_{Fe}) formed in the ultrathin Co–Fe LDHs led to multifarious orbital and electron distributions, a lower Co coordination number, and improved structural disorder. Impressively, the as-prepared electrocatalyst showed a low OER $E_{j\,=\,10}$ of 1.496 V. Wang et al. grew Ni–Fe LDH nanoarrays on electronegative Au-loaded Ni foam (Ni–Fe LDH@Au/Ni) for the OER [66]. Working as an electron adsorbate, the highly electronegative Au stabilized and generated Ni cations with a high oxidation state (Ni^{3+}), which facilitated the formation of the intermediate hydroperoxyl species (OOH*). Consequently, Ni–Fe LDH@Au/Ni exhibited superior OER performance with an $E_{j\,=\,100}$ as low as 1.473 V.

3.1.5. Transition metal chalcogenides

Transition metal chalcogenides (TMChs) have a general formula of M_xX_z, in which M is the metal element and X is the chalcogen element (X = S, Se, Te). Monochalcogenide MX, dichalcogenide MX_2, heazlewoodite M_3X_2, and pentlandite M_9X_8 are the most common stoichiometries of TMChs. The large structural diversity renders TMChs highly interesting for oxygen electrocatalysis [67]. Different electronic engineering strategies have been adopted to illustrate the relationship between TMCh structure and intrinsic activity, which could serve as significant guidance for optimal catalyst design. Exposing the edge sites and introducing lattice defects are two efficient approaches to improve TMChs' catalytic activities. For example, Song et al. explored V-doped pyrite NiS_2 nanosheets as an OER catalyst [66]. After V-displacement defects were engineered, the reconfigured electronic structure enabled pyrite NiS_2 to change from semiconductive to metallic characteristics, due to electron transfer from doped V to Ni sites. The metallic V-doped NiS_2 nanosheets exhibited outstanding OER performance, with a small overpotential of 290 mV and long-term stability (20 h) in 1 M KOH electrolyte. As another promising route, strain engineering can efficiently manipulate the electronic structure of TMChs. For example, Deng *et al.* reported a series of lattice-strained NiS_xSe_{1-x} nanosheets@nanorods [68]. Experimental and calculation results revealed that the lattice strain led to a narrowed d-band width and a shift of the d-band center toward the E_f. As a result, $NiS_{0.5}Se_{0.5}$ with around 2.7% lattice strain exhibited a high OER performance (overpotential of 257 mV at 10 mA cm^{-2}) and ultra-long stability (more than 300 h). Chalcogenide materials beyond transition metals and layered metal oxyhydroxides, such as GaSe, GeS, and NiO(OH), have also been studied for both the ORR and the OER due to their inherent electrochemical activities [58,67].

3.2. Single-atom catalysts

As emerging oxygen catalysts, SACs have the merits of low cost, maximum metal utilization, superior catalytic selectivity/activity, and structural flexibility. Typically, SACs consist of atomically dispersed transition metal centers (e.g., Ni, Co, Fe, and Mn) and several in-plane coordinated atoms (C, N, or O) immobilized in the carbon matrix [14]. In addition, heteroatoms (B, O, S, and P), known as environmental atoms, can also be incorporated into the carbon matrix. In unsaturated coordination conditions, the center metal generally acts as the active site and is able to interact with guest species (Fig. 4e) [69]. The antibonding states produced from coupling between the metal d-orbitals and the O *2p*-orbitals in oxygen intermediates downshift the energy, weakening the M−O bonding. Hence, the lower the metal d-band center, the weaker will be the bonding strength of oxygen species to the metal atom.

During the ORR process, the metal d-orbitals interact with the oxygen p electrons, enabling the adsorption of O_2 and the subsequent electron transfer [70]. The d-band structure for the center metal atoms is one of the most important descriptors for indicating the intrinsic activities of SACs. Recently, Zeng et al. comprehensively calculated the intrinsic ORR activities of SACs made of 28 kinds of center metal atoms [71]. Plots of theoretical onset potential (E_{onset}) vs. ΔG_{OH^*} for different SACs exhibit an interesting volcano shape, in which Fe lies on the volcano top with different N coordination configurations (i.e., pyrrole-4N or pyridine-4N coordination) (Fig. 5a). The plots provide a universal design principle to select the center metal atoms for highly efficient electrocatalysts. Moreover, Liao et al. experimentally studied the ORR performance of SACs based on Fe, Co, Ni, Mn, and Cu [72]. Their results indicated that the ORR activities followed the sequence Fe > Co > Cu > Mn > Ni (Fig. 5b). Huang and Duan et al. demonstrated a general method to embed various atomically dispersed transition metal atoms (e.g., Fe, Co, and Ni) into nitrogen-doped graphene for the OER [73]. The MN_4C_4 moieties were recognized as active sites with an OER activity trend of Ni > Co > Fe.

Apart from the metal center, the local coordination structure is also important for determining the catalytic properties. The center metal atoms are normally coordinated by several non-metal atoms via d–p σ-bonds as well as possible back-donating p-bonds. In this regard, the electronic structure, especially the d electrons, of the center metal atoms in SACs can be regulated by changing the surrounding environment of the metal atoms using different approaches, including heteroatom doping, coordination number control, and heterostructure construction [69]. Moreover, SACs on various 2D materials, such as MXenes, layered oxides, and LDHs, have aroused increasing interest recently due to the tunable electron density and bandgap of 2D supports and uniform geometry of the supported SACs' active sites [74]. Several other manipulation approaches have also emerged to enhance SAC catalytic performance, such as creating edge-hosted MN_{2+2} sites (M = Fe, Co) [75], and controlling morphology and active site distribution [76].

3.3. Metal-free catalysts

Carbon-based metal-free materials, including carbon nanotubes, graphene, graphitic carbon nitride (g-C_3N_4), and their analogues, are intensively investigated for electrochemical applications due to their high conductivity and huge surface area [80,81]. The catalytic activity of carbon-based metal-free materials originates from the electron redistribution induced by either dopants or intrinsic carbon defects (e.g., vacancies, non-hexagonal carbon rings, edges, and adsorbed molecules). Therefore, to obtain superior electrocatalytic performance, heteroatom doping or defect creation are generally employed to modify the electronic structure and trigger charge redistribution in the carbon matrix [82].

3.3.1. Heteroatom-doped carbon materials

Doping increases the catalytic activity of carbon electrocatalysts by forming defects, enhancing electronic conductivity, and optimizing the intrinsic electronic properties of the carbon network. N-doped carbon materials are the most widely investigated metal-free electrocatalysts, with the doping of N into the carbon matrix efficiently modifying the electron distribution of the surrounding C atoms [83,84]. Pioneering work on the study of N-doped coaxial carbon nanocables (denoted as

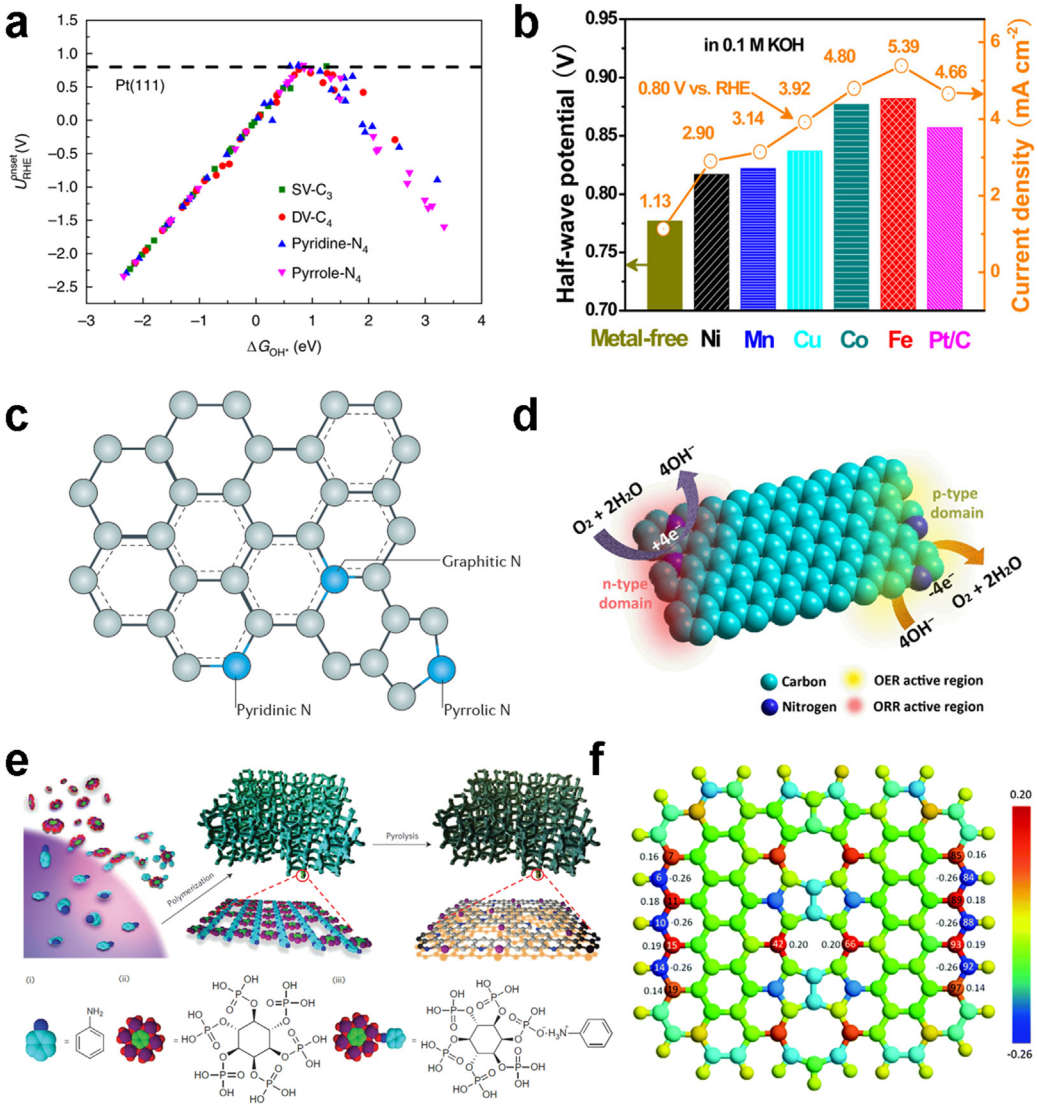

Fig. 5. (a) ORR theoretical E_{onset} vs. adsorption free energies ΔG_{OH^*} of SACs based on different transition metal atoms. Reproduced with permission [71]. Copyright 2018, Springer Nature. (b) Halfwave potential ($E_{1/2}$) of SACs based on various metal elements, obtained from linear sweep voltammetry in the presence of O_2-saturated 0.1 M KOH electrolyte. Reproduced with permission [72]. Copyright 2014, American Chemical Society. (c) Different doped N configurations in N-functionalized carbon. Reproduced with permission [28]. Copyright 2016, American Association for the Advancement of Science. (d) Schematic of the ORR and OER at various active sites on the n- and p-type domains of the NGRW catalyst. Reproduced with permission [77]. (e) Schematic of the preparation process for NPMC foams. Reproduced with permission [78]. Copyright 2015, Nature Publishing Group. (f) Charge density distribution of different defects on carbon material. Reproduced with permission [79]. Copyright 2017, Wiley-VCH.

CNT@NCNT) was reported by Wei et al. [85]. The CNT@NCNT was equipped with rich surficial N atoms acting as the active sites and well-preserved inner CNTs promoting the electron transfer. Compared with pristine CNTs, CNT@NCNT delivered much larger ORR current densities, about 51 mV positively shifted ORR onset potential, and lower peroxide formation, together with smaller OER overpotential and larger OER current densities.

Several N configurations were proposed in an N-doped graphite plane, including pyridinic, graphitic, and pyrrolic N (Fig. 5c) [28]. Different N configurations can influence the electronic structure of adjacent C atoms to varying degrees, resulting in different catalytic performance. However, whether the graphitic or pyridinic N works as the main OER active site is still under debate. In this regard, identifying the detailed mechanism whereby different N configurations promote the catalytic activities of carbon materials would be very useful [17]. As a representative example, Liu et al. fabricated N-doped three-dimensional graphene nanoribbon as an oxygen bifunctional electrocatalyst [77]. The electron-donating quaternary N was experimentally proven to dominate the ORR activity, while the electron-withdrawing pyridinic N moieties acted as OER active sites (Fig. 5d).

Other kinds of heteroatoms (e.g., B, P, and S) have also been adopted to improve the catalytic activities of carbon nanomaterials. With respect to B doping, the introduction of B increased the quantity of hole-type charge carriers because the electropositive B atoms facilitated chemisorption with electronegative oxygen species [86]. P doping created defect-derived surfaces for oxygen adsorption because P has a lower electronegativity and larger atomic size than C [87,88]. The large size of the S atom makes it much more challenging to dope than N. The improved catalytic activity with S doping was ascribed to the spin distributions, since the charge polarization originating from the electronegativity difference between S (χ = 2.58) and C (χ = 2.55) was negligible [89,90].

Doping carbon materials with multiple types of heteroatoms has also been verified as an efficient strategy to facilitate electrocatalytic activity [78,91–93]. For instance, N, P co-doped porous carbon foam was demonstrated to be an effective oxygen bifunctional electrocatalyst

(Fig. 5e), exhibiting an ORR $E_{1/2}$ of 0.85 V vs. RHE together with a smaller OER onset potential than RuO_2 [78]. Theoretical calculations confirmed the co-doping role of N and P at the graphene edge in boosting both ORR and OER activities by lowering the reaction energy barrier.

3.3.2. Defect-rich carbon materials

In carbon materials, defects, including topological (e.g., pentagonal, heptagonal carbon ring) and edge defects, have been confirmed as significantly involved in the oxygen electrocatalytic reactions [79,94]. Defects optimized the charge/spin distribution of the carbon materials with sp^2-conjugation, facilitating the chemisorption of intermediates, promoting electron transfer, and enhancing catalytic activity (Fig. 5f) [79]. However, in real cases, doping and edge sites always coexist with other types of crystalline disorder. The local electron density of carbon can be redistributed by both heteroatom dopants and edge-induced topological defects, and this redistribution benefits the adsorption of O intermediates. It has also been demonstrated that doping carbon materials at the edge or defect sites is an efficient approach to boost oxygen electrocatalytic activities. A syncretic understanding is highly desired to guide metal-free carbon catalyst design. Thus, carbon materials with rich defects have been extensively studied as oxygen catalysts over the decades [95–97]. However, the large OER overpotentials of metal-free catalysts remain critical restrictions for commercial applications.

4. Electronic structure regulation strategies

4.1. Heteroatom doping

Heteroatom doping into pristine materials tends to induce local structural distortion and electron redistribution owing to differences between the atomic size and electronegativity of the substituted atoms and the receiving materials. Local structural changes make the doping atoms or neighboring atoms superior catalytic sites and facilitate charge transfer from the active sites to the adsorbed reactants [23,98]. Based on the doped elements, doping is classified into cationic and anionic. Since transition metal atoms usually possess empty d orbitals and act as electrophilic sites, cationic doping has been widely used to optimize the energy levels of active sites and adjust their key oxygen intermediate adsorption strength. Conversely, anionic doping (e.g., C, N, O, P, and S) has been applied to regulate the local electron distribution and enhance electrocatalytic activity toward the OER [99].

As replacements for noble metal elements in oxygen catalysts, transition metal compounds have aroused tremendous interest because of their good stability and catalytic activity. Nevertheless, most transition metal compounds are semiconductors with low conductivity, which hampers their practical catalytic performance. In this regard, doping has been intensively explored for transition metal compounds to tailor their electronic structures and catalytic activities [100]. In a representative example, Gao et al. synthesized Co-doped NiO nanoflakes (denoted as Co–NiO) as an efficient ORR catalyst in an alkaline solution [101]. The conductivity of Co–NiO was apparently increased owing to the occupied electronic state at the E_f induced by the Co dopant. Therefore, compared to pristine NiO, Co–NiO exhibited obviously enhanced ORR performance, with an E_{onset} of 0.92 V vs. RHE and an $E_{1/2}$ of 0.79 V vs. RHE. Similarly, the ORR activities of many other transition metal compound-based electrocatalysts (e.g., TMNs, TMPs, and TMSs) could also be substantially improved by the cationic doping strategy [99].

Doping with heteroatoms is also a powerful approach to regulate the electronic structures of OER catalysts. For instance, Huang et al. studied site-selective Fe doping in $NiCo_2O_4$ tetrahedral sites (denoted as NiCoFeO) [102]. The σ-bonds originating from TM-*3d*-e_g and O-*2p* orbital hybridization determined the electronic structure of the catalyst with the O intermediates during the OER process. As revealed by the total DOSs of NiCoFeO and NiCoO (Fig. 6a), Fe doping enhanced the electronic states near the E_f, indicating the boosted driving force of oxygen exchange between surface cations and O_2^{2-}/O^{2-} adsorbates during the OER. This observation implied that Fe doping increased the carrier density and improved the intrinsic conductivity of the catalyst. Moreover, Fe was preferentially doped into the tetrahedral sites of NiCoO, which induced dense OER-active Ni^{3+} and Co^{2+} at the octahedral sites. In addition, the e_g electron number was 1.53 for NiCoFeO, which was closer to 1 than 1.62 for NiCoO. As a consequence, NiCoFeO exhibited significantly enhanced OER activity, with an ultralow $E_{j\ =\ 10}$ of 1.431 V and a small Tafel slope of 39 mV dec^{-1}.

In addition to cationic doping, anionic doping (e.g., C, N, O, P, and S) has also been utilized to intrinsically enhance the conductivity of transition metal compounds and optimize the adsorption capability of O intermediates [107–109]. As the ionic radii of anions are generally bigger than those of metal cations, anionic doping can generate significant alterations in local structure, thus inducing obvious changes in O-intermediate adsorption/desorption. For example, Song et al. demonstrated that the doping of low-electronegative P atoms in MoS_2 nanosheets generated significantly improved ORR activity, with a 7-fold current density increase and a large positive shift of 160 mV for both E_{onset} and $E_{1/2}$ [110].

When it comes to SACs, the active site generally consists of an isolated metal atom coordinated with non-metal atoms (C or N) via d–p orbital hybrid σ-bonds and back-donating p-bonds. The unique coordination structures of SACs dominate their catalytic performance and efficiency [111]. Importantly, the electronic structure of SACs (especially the d-orbital electrons of center metal atoms) can be regulated by doping metal or non-metal elements into the surrounding environment adjacent to the center metal atoms [69]. Metal-doped SACs can be viewed as derivative structures of SACs, featuring dual metal atoms coordinated adjacently with strong intermetallic interaction and charge polarization. The d–d orbital hybridization between metal atoms, as distinct from the d–p orbital hybridization between metal atoms and non-metal atoms, offers a new mechanism to optimize the electronic structure of SACs [112]. The active sites are the dual metal atoms, which not only maximize the atomic utilization efficiency but also enable fast reaction kinetics with optimal reaction pathways [113]. For instance, SACs containing dual-metal Fe–Co sites coordinated by six N atoms in carbon nanotubes (denoted as (Fe, Co)/CNT) reached a high ORR activity, with an E_{onset} of 1.15 V and an $E_{1/2}$ of 0.954 V [114]. Compared with single Co atoms (denoted as Co/CNT-C) and single Fe atoms (denoted as Fe/CNT-C), (Fe, Co)/CNT promoted the activation of O_2 through weakening the oxygen-oxygen double bonds Bifunctional oxygen catalytic activities were also demonstrated for other bimetallic SACs, such as Ni–Co SAC [115], Ni–Fe SAC [116], and Zn–N–Co SAC [117].

Non-metal atom doping (e.g., B, P, and S) in SACs can trigger high activity by affecting the electron density over the metal centers. Among all the non-metal elements, S has been revealed as a highly effective dopant [118–120]. Because S has a lower electronegativity (2.58) than N (3.04), electrons tend to transfer from S to N atoms once the S–N bond is formed [70]. Zhang et al. synthesized S-doped Fe-, Co-, and Ni-based SACs and explored their ORR activities [121], finding that S doping in Fe-based SAC resulted in well-dispersed FeN_4S_2 center sites, while S-doped Co-based and Ni-based SACs generated CoN_3S_1 and NiN_3S_1 sites due to the direct replacement of S by N. Electrochemical measurements indicated that FeN_4S_2 had the best ORR performance in alkaline solution, showing an E_{onset} of 1.00 V vs. RHE and an $E_{1/2}$ of 0.87 V vs. RHE, which were much higher than for CoN_3S_1 (E_{onset} of 0.95 V and $E_{1/2}$ of 0.86 V vs. RHE) and NiN_3S_1 (E_{onset} of 0.96 V and $E_{1/2}$ of 0.82 V vs. RHE). The prominent effect of S coordination in FeN_4S_2 came from the electron transfer from S to N, enabling positively charged S and negatively charged N. Consequently, the electron density of the center Fe increased, which in turn enhanced the ORR activity. Moreover, compared with CoN_3S_1 and NiN_3S_1, FeN_4S_2 possessed the highest DOSs near the E_f, expediting the ORR RDS (i.e., the reduction of OH* to OH^-). This phenomenon indicated the greatly improved electron transfer of FeN_4S_2, which further accounted for the enhanced conductivity and catalytic

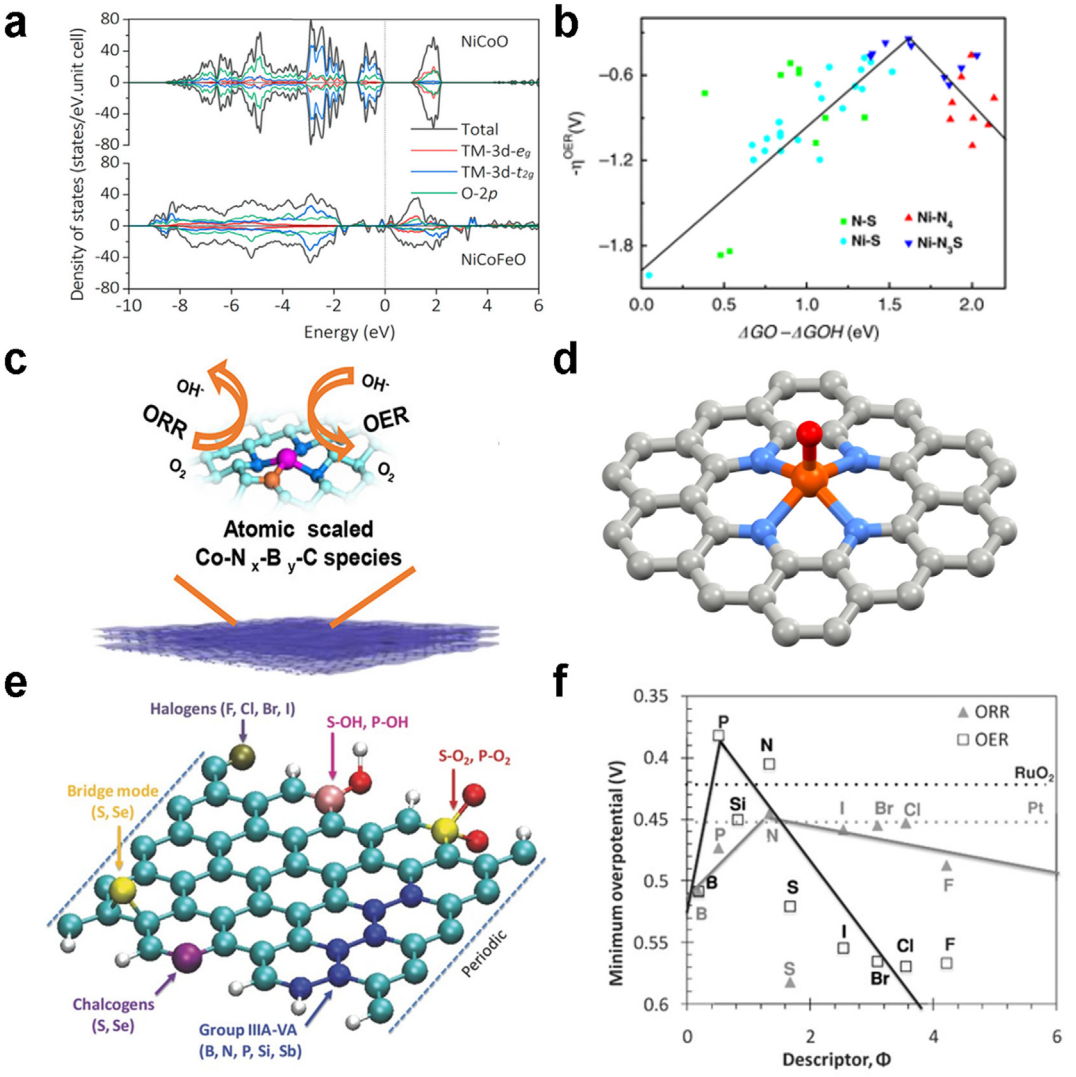

Fig. 6. (a) Calculated partial density of states (PDOSs) of bulk NiCoO and NiCoFeO. Reproduced with permission [102]. Copyright 2019 American Chemical Society. (b) OER volcano plots of the overpotential η vs. the difference between the adsorption free energy of O* and OH* for different models. Reproduced with permission [103]. (c) Schematic of B-doped Co–N–C SAC for bifunctional oxygen electrocatalysis. Reproduced with permission [104]. Copyright 2018, American Chemical Society. (d) Schematic structure of pentacoordinated-Zr catalyst with axial O ligand for the ORR. Reproduced with permission [105]. Copyright 2022, Wiley-VCH. (e) Schematic of the X-doped graphene nanoribbons, demonstrating the possible positions of dopants. Reproduced with permission [106]. Copyright 2015, Wiley-VCH. (f) The minimum ORR/OER overpotentials vs. the descriptor Φ for X-doped graphene. Reproduced with permission [106]. Copyright 2015, Wiley-VCH.

performance. Additionally, the calculated PDOS of Fe, Co, or Ni atoms in SACs revealed that metal d-orbitals contributed to the enhanced DOS in FeN_4S_2, CoN_3S_1, and NiN_3S_1. Recently, Feng et al. developed an S-doped Ni SAC as an OER catalyst [103]. Theoretical investigation showed that S atoms in the Ni–N_3S model acted as electron donors and decreased the electron donation of Ni atoms to the neighboring N atoms. Thereby, the S dopant effectively tuned the hybridization states between Ni atoms and the neighboring N atoms, which improved the local electronic states of the single-atom Ni site and boosted the OER activity (Fig. 6b). As a consequence, the S-doped Ni SAC electrocatalyst exhibited a low OER overpotential of 0.28 V at 10 mA cm^{-2} and a small Tafel slope of 45 mV dec^{-1} in 1 M KOH.

In addition to S, B and P dopants have also been adopted to tune the electronic structures of SACs. For instance, Chen et al. developed P-coordinated Fe-based SAC (FeN_3P) for the ORR and OER. Interestingly, FeN_3P showed better catalytic performance than FeN_4 due to the reduced RDS energy barrier (i.e., from OH* to OH^-) [122]. As a result, FeN_3P demonstrated a larger limited current diffusion density (J_L = 5.66 mA cm^{-2}) and a more positive E_{onset} of 0.941 V and $E_{1/2}$ = 0.867 V vs. RHE compared with other counterparts. Moreover, FeN_3P displayed a low OER potential of 1.66 V vs. RHE at 10 mA cm^{-2} ($E_{j\ =\ 10}$), which was close to that of RuO_2 (1.61 V vs. RHE). The potential gap (ΔE) between $E_{j\ =\ 10}$ and $E_{1/2}$ normally is an important indicator of bifunctional activity. Importantly, FeN_3P showcased a small ΔE of 0.79 V, comparable to that of Pt/C + RuO_2 (0.76 V). The enhanced performance arose from asymmetric N/P coupling on Fe active sites, which resulted in the optimal charge distribution and electronegativity of these sites.

A bifunctional oxygen electrocatalyst was proposed using B-doped Co-based SAC [104]. The ΔE of the B-doped Co-based SAC in 0.1 M KOH was only 0.83 V ($E_{j\ =\ 10}$ of 1.66 V vs. RHE and $E_{1/2}$ of 0.83 V vs. RHE). B doping was found to induce unbalanced charge distribution in Co–N–C, N–C, and C–B moieties, which favored the adsorption of oxygen intermediates with the side-on mode and thus accelerated the $4e^-$ reaction kinetics for the ORR and OER (Fig. 6c). Recently, introducing O atoms into SACs has also been adopted to regulate the electronic structure and improve the electrocatalytic performance of SACs [123]. For instance, our group demonstrated that after introducing nontrivial axial O ligands into Zr-based SAC (O–Zr–N–C) (Fig. 6d), the d-band center of Zr was obviously downshifted, conferring upon Zr single atom sites a stable

coordination structure and suitable adsorption strength for O species [105]. Therefore, the ORR performance of O–Zr–N–C significantly surpassed that of commercial Pt/C, with an $E_{1/2}$ of 0.91 V vs. RHE and excellent durability for 130 h of operation. Furthermore, due to the axial O ligand on the Zr site, O–Zr–N–C was highly resistant to aggregation, enabling the fabrication of O–Zr–N–C with high single-atom Zr loading (9.1 wt%).

In the case of metal-free carbon-based materials, non-metal doping provides extra p-orbital electrons to carbon atoms and creates electron-donating/accepting sites according to the electronegativity of carbon and doping atoms. The redistribution of p-orbital electrons caused by heteroatom doping facilitates the adsorption of O species and electron transfer between the active sites and O intermediates. Hence, heteroatom doping (including single-element doping and multi-element doping) has been intensively employed to modify the electronic structures of carbon materials for catalytic oxygen reactions. For instance, Xia et al. used DFT calculations to systematically investigate the effect of doping various heteroatoms into carbon-based catalysts [106]. The doping positions of different dopants — i.e., X (X = B, N, F, Si, P, S, Cl, Se, Br, Sb, I, POH, PO_2, SOH, SO_2, and SeO_2) — are illustrated in Fig. 6e. The electronegativity multiplied by the electrical affinity of dopants was used as the intrinsic descriptor (Φ) to correlate with the oxygen intermediates' (e.g., OH* and OOH*) adsorption energy. This study revealed that the active sites generated through doping carbon materials with p-block elements were the C atoms close to the dopants. Carbon materials doped by elements with $\Phi < 1$ (e.g., B, Si, P, and Sb) were the ORR active catalysts. When it came to X–O_2 and X–OH doping (X = S, P), the catalytic active sites were the dopants themselves. The results also indicated that edge-site doping of graphene nanoribbons was a highly efficient method for developing metal-free carbon-based bifunctional oxygen catalysts (Fig. 6f).

4.2. Vacancy creation

Vacancies are typical lattice defects in crystalline materials, meaning lattice positions that are vacant due to the absence of atoms. Vacancies can cause the redistribution of the local electron density and increase the DOS near the E_f [124–126]. Consequently, the presence of vacancies in catalysts enables researchers to regulate electron configuration, change element valence, improve charge transfer properties, and thus optimize intrinsic electrocatalytic activity [127,128].

With respect to transition metal compounds, anion vacancies can change the intrinsic stoichiometric ratio and cause a distorted local electric field, affecting the electronic properties of metal atoms adjacent to the vacancy sites in terms of valence state and e_g electrons [134]. O vacancies are the most common anion vacancies in TMOs due to their low formation barrier. The physicochemical properties of TMOs can be significantly altered as a result of O vacancies. For instance, Qiao et al. synthesized 1D single-crystal CoO with O vacancies (SC CoO NRs) as an efficient ORR catalyst (Fig. 7a) [129]. O *1s* XPS and O–*K* edge XAS spectra suggested enrichment of the O vacancies on the surface of SC CoO NRs. This structural feature of SC CoO NRs was further verified by the noticeable peak shift in the Co-$L_{2,3}$ edge towards low photon energy and in the Co *2p* XPS spectrum towards low binding energy, which originated from electron transfer from the O vacancies to the Co d band. Thus, a combination of the XPS and XAS results provided solid evidence for the abundant O vacancies on the surface of CoO. Moreover, DFT calculation revealed that the O vacancies on the CoO (111) facets induced new electronic states in the bandgap by the hybridization of O-*2p*, Co-*3d*, and Co-*3s* orbitals (Fig. 7b), which, in turn, improved the electronic conductivity and electrocatalytic activity of the fabricated CoO catalyst. Therefore, SC CoO NRs showed an E_{onset} of 0.96 V vs. RHE, an $E_{1/2}$ of 0.85 vs. RHE, and a Tafel slope of 47 mV dec^{-1}, which approached the values of Pt.

Many studies have reported that defects in transition metal compounds greatly improved OER performance [135]. For example, Zheng's group synthesized mesoporous Co_3O_4 nanowires with abundant O vacancies by using $NaBH_4$ as the reductant [125]. Compared with pristine Co_3O_4, the oxygen-deficient Co_3O_4 exhibited a higher current density of 13.1 mA cm^{-2} at 1.65 V vs. RHE and a lower E_{onset} of 1.52 V vs. RHE for the OER. DFT calculations suggested that O vacancies caused the generation of new gap states, in which the electrons previously related to the Co–O bonds were delocalized, leading to enhanced electrical conductivity and electrocatalytic performance. In addition to TMOs, anion vacancies were also demonstrated to be effective for boosting the ORR and OER performance of other metal compounds (e.g., TMDs, TMNs, TMChs, and TMPs) [136,137].

Apart from anion vacancies, cation vacancies have also been shown to significantly affect the physicochemical properties of transition metal compounds. Nevertheless, the huge formation energy of cation vacancies makes it challenging to create an abundance of them. A few approaches have been developed to prepare metal compounds with cation vacancies. For example, Shao and co-workers created A-site cation deficiency in $LaFeO_3$ perovskite oxides (denoted as $La_{1-x}FeO_{3-\delta}$) by a sol-gel process to improve the ORR/OER activities (Fig. 7c) [130]. Their results disclosed that A-site cation deficiency helped to form a small amount of Fe^{4+} with an optimal e_g orbital filling ($t_{2g}^3e_g^1$), which contributed to promoting the electrocatalytic processes based on Shao-Horn's principle [32]. $La_{1-x}FeO_{3-\delta}$ showed outstanding ORR and OER activities, with a ΔE of 1.06 V. This finding provided a new method to enhance the catalytic activity of perovskites and guide future studies to design efficient electrocatalysts.

Cation vacancies can easily be generated on the surface of ultrathin nanosheets because of the low atom-escape energy at the surface sites. Recently, Xie et al. controlled cobalt vacancies in ultrathin $CoSe_2$ nanosheets [138]. Specifically, diethylenetriamine (DETA) was used to coordinate with Co complexes. After ultrasonication treatment, DETA triggered Co atoms to detach from the $CoSe_2$ lattice, inducing the formation of cobalt vacancies in the ultrathin $CoSe_2$ nanosheets. Theoretical calculations revealed that the H_2O adsorption energy on the cobalt vacancy sites of $CoSe_2$ was substantially higher than on the Co sites in bulk $CoSe_2$. The calculation results suggested that cobalt vacancies in the ultrathin $CoSe_2$ served as active sites to efficiently catalyze the OER, which displayed a low $E_{j\ =\ 10}$ of 1.55 V in a pH = 13 electrolyte.

The metal center of SACs is normally considered to be coordinated with four N atoms. However, such a coordination configuration may not exhibit optimal bonding strength for O species during oxygen electrocatalysis. Creating a nontrivial type of "vacancy" for SACs via removing the coordination atoms of the metal center offers a viable way to optimize the ORR/OER performance of SACs. For example, Zhuang et al. synthesized a Fe-based SAC through the HNO_3 treatment of carbon black in the presence of Fe [139]. The local structure–activity relationship of various active sites was assessed both experimentally and theoretically, showing ORR activity decreasing in the order Fe–N_2–C > Fe–N_4–C > Fe_4–N–C > N–C ≫ Fe_4–C ≥ C. Compared to the typical Fe–N_4–C structure, Fe–N_2–C located at the edge site offered a more favorable O_2 adsorption energy and higher ORR activity.

Defect engineering was also used to render a group of ORR-inactive SACs active [131]. Specifically, Chen and co-workers calculated the OH* adsorption energy barrier on the main group metal-based SACs (i.e., MgN_4C, AlN_4C, and CaN_4C) and found that ORR activity was severely hampered by the tight bonding of the metal centers. However, the Mg-based SAC with reduced N coordination (i.e., MgN_2C) enabled near-optimal adsorption strength for O intermediates (Fig. 7d). Impressively, MgN_2C showed superb ORR activity, with an $E_{1/2}$ of 0.91 V RHE, an E_{onset} of 1.03 V vs. RHE, and a Tafel slope of 62 mV dec^{-1}.

Besides coordination vacancies, carbon vacancies created by removing C atoms near the M–N_x site can also improve the intrinsic electrocatalytic activities of SACs. For instance, Xu et al. fabricated an edge-rich Fe-based SAC (Fe/OES) for ORR catalysis [140]. Fe/OES exhibited abundant meso/micropores with dense three-phase interfaces for rapid reactant transportation to Fe sites, enabling the ultrahigh utilization of active sites. As expected, Fe/OES promoted the ORR process, yielding a higher E_{onset} (1.0 V vs. RHE) and $E_{1/2}$ (0.85 V vs. RHE) than the

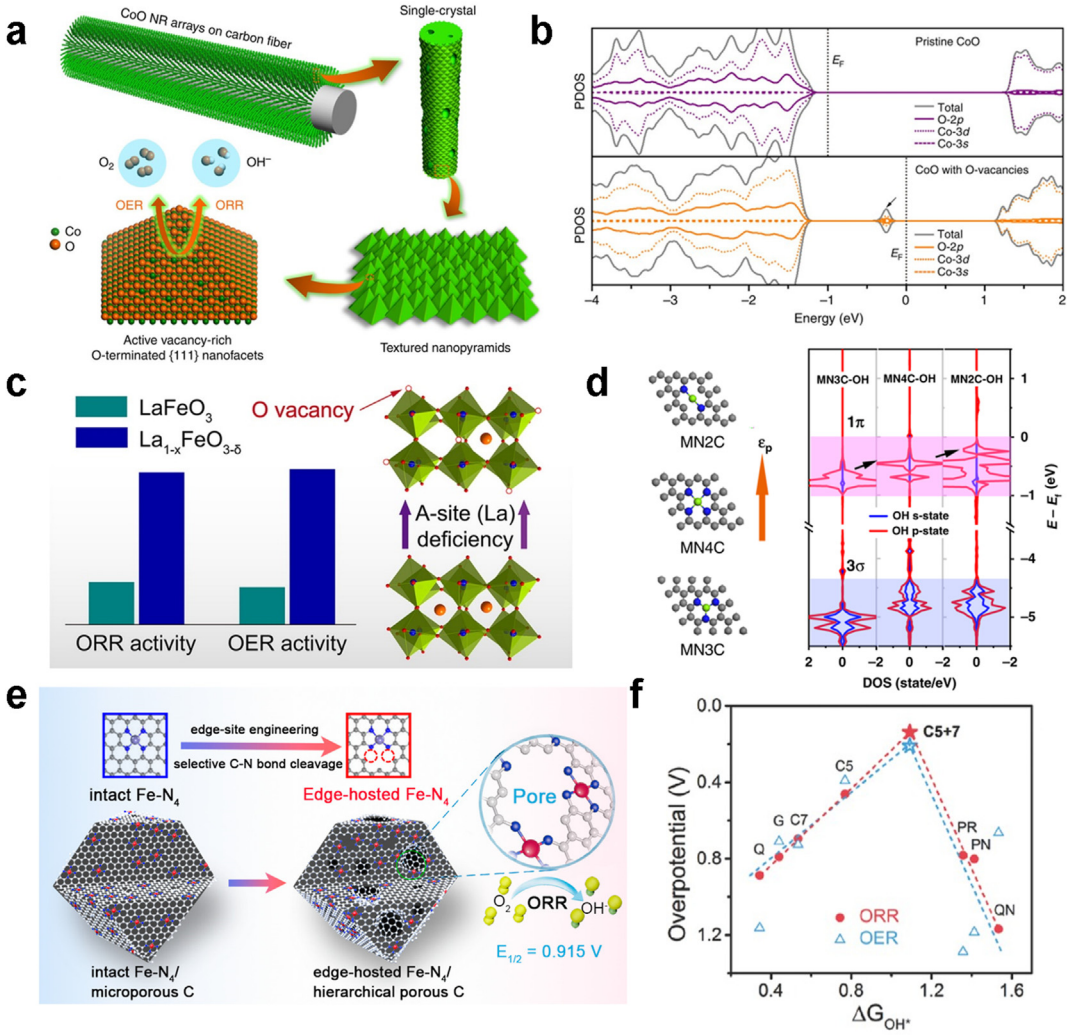

Fig. 7. (a) Schematic illustration showing the fabrication of vacancy-rich O-terminated CoO nanorods. (b) PDOS of pristine CoO and oxygen-deficient CoO. Reproduced with permission [129]. (c) Schematic illustration showing the formation of O vacancy and Fe^{4+} in A-site-deficient $La_{1-x}FeO_{3-\delta}$ and comparing its ORR/OER activity with that of $LaFeO_3$. Reproduced with permission [130]. Copyright 2016, American Chemical Society. (d) The Mg cofactors' geometries in different N-coordinated environments that tune the ε_p of Mg atoms, and the corresponding DOS of OH after interaction with the p-state of Mg. Reproduced with permission [131]. (e) Schematic illustration of the fabrication of edge-hosted Fe–N_4 moieties with C vacancies. Reproduced with permission [132]. Copyright 2018, American Chemical Society. (f) ORR/OER volcano plots showing the overpotential vs. adsorption energy of OH*. Reproduced with permission [133]. Copyright 2016, Wiley-VCH.

control samples. Wang's group investigated the effect of various C vacancies on the ORR over a series of Fe–N_4 models (FeN_4, FeN_4-6r-c1, FeN_4-5r-c1, FeN_4-6r-c2, and FeN_4-5r-c2; 6r or 5r refers to six- or five-membered heterocycle ring, and c1 or c2 refers to the cleavage of one or two C–N bonds next to Fe–N_4) (Fig. 7e) [132]. Among the five models, FeN_4-6r-c2 exhibited the lowest energy barrier for the overall ORR reaction, superior to FeN_4 sites without C vacancies.

The OER performance of SACs can also be affected by C vacancies. For example, Lee et al. developed a series of edge-hosted SACs based on different transition metals (Fe, Co, Ni, Cu) [141]. Impressively, the Fe-based catalyst provided superior ORR ($E_{1/2}$ of 0.91 V vs. RHE) and OER activity ($E_{j=10}$ of 1.6 V) and stability (12 h of operation). DFT calculations proved that the edge-hosted Fe–N_2 model greatly promoted the desorption of OH* in the ORR, enabling a more favorable ORR pathway than the bulk-hosted Fe–N_4. In the OER process, the edge Fe–N_2 model allowed a RDS ($O^* + OH^- \rightarrow OOH^* + e^-$) with a close ideal adsorption energy barrier of 3.15 eV and a theoretical OER overpotential of 0.579 V.

In carbon-based metal-free materials, topological defects (e.g., pentagon (C5), heptagon (C7), and octagon (C8)), which can be viewed as results of carbon vacancies in the perfect graphitic structure, also play significant roles in oxygen reactions [79,94]. Wei et al. fabricated nitrogen-doped edge-rich graphene mesh (denoted as NGM) to study the origin of ORR and OER electrocatalytic activity in carbon materials [133]. The NGM catalyst demonstrated excellent electrocatalytic performance for both the ORR and the OER, with an ORR E_{onset} of 0.89 V vs. RHE, an $E_{1/2}$ of 0.77 V vs. RHE, and an OER $E_{j=10}$ of 1.67 V vs. RHE. In addition, experimental and first-principles simulations revealed the critical role of topological defects in determining the activity of metal-free carbon-based electrocatalysts. A nitrogen-free configuration with adjacent C5 and C7 carbon rings exhibited the lowest overpotential, i.e., 0.14 V for the ORR and 0.21 V for the OER (Fig. 7f). In addition, a defective carbon catalyst doped with B and N (B, N-carbon) was constructed as an excellent metal-free bifunctional electrocatalyst for the ORR and OER [142]. Due to rich carbon defects, B, N-carbon exhibited superb bifunctional activity, with a ΔE of 0.712 V.

4.3. Strain induction

Strain is caused by the crystal lattice deformation associated with an external force. Strain induction is a powerful way to regulate the

metal–oxygen bonding strength by tuning the energy level of the d-band. Fig. 8a illustrates the correlation between the metal d-band structure and surface strain [143]. Compared with the late transition metals, early transition metals with less than half-filled d-bands show weaker interaction with adsorbates upon lattice expansion. This apparent phenomenon can be clarified by the classical d-band model. In detail, an expanded strain reduces the wave function overlap, which further narrows the d-band of the metal. For late transition metals, narrowing the d-band increases its population, so the d-band center is lifted to preserve d-band filling. For early transition metals, the expanded strain downshifts the metal d-band center. This observation suggests that the catalytic activity can be adjusted by tuning the surface strain of the catalyst according to the above d-band model. Based on the theory, the electrochemical Li^+ intercalation/extraction method was used to continuously control the lattice strain of a platinum (Pt) catalyst from compressive to tensile in order to readily tune the catalyst's ORR activity (Fig. 8b) [144].

Besides shifting the metal d-band center, strain induction can finely regulate the e_g orbital splitting and polarization in perovskites and other TMOs. Lee and co-workers synthesized strained $LaNiO_3$ (LNO) for bifunctional ORR/OER catalysts by adjusting the strain from −2.2% to 2.7% through applying different lattice-mismatched substrates (Fig. 8c) [145]. When $LaAlO_3$ substrate was used, a compressive strain from −1.2 to 0% was obtained by changing the thickness of LNO on $LaAlO_3$. The bifunctional activity of LNO was found to increase drastically with the compressive strain. They weighted the center of each orbital state to its orbital occupancy to calculate the e_g center (E_{eg}). Interestingly, due to disparate polarization to the d_{z^2} orbital, the M−O strength was disproportionate to that of $d_{x^2-y^2}$, which was in agreement with a geometric argument postulating greater overlap between O *2p* orbitals and the d_{z^2} states. By examining both orbital splitting and polarization at the surface of LNO, the authors established E_{eg} as a new descriptor to predict strain-induced effects for the ORR and OER activities of perovskites and related TMOs.

The catalytic performance of SACs has also been tailored by strain regulation. Recently, Shen *et al.* used DFT calculations to evaluate how the strain in Co, N co-decorated graphyne (denoted as Co@N_1-GY) affected the OER activity (Fig. 8d) [146]. The result suggested that from compressive strain to tensile strain, the C–Co bond length was increased linearly, and the d-band center of Co and the p-band center of C were upshifted linearly (Fig. 8e). In addition, the compressive strain would result in large interaction between the O species and the active sites, partially because of the structural distortion caused by the surface compressive strain during O-intermediate adsorption. In this regard, adsorption–desorption energetics toward the O intermediate could be finely tuned under the applied tensile strain. Consequently, the adsorption of oxygen species in the OER became weaker and weaker from

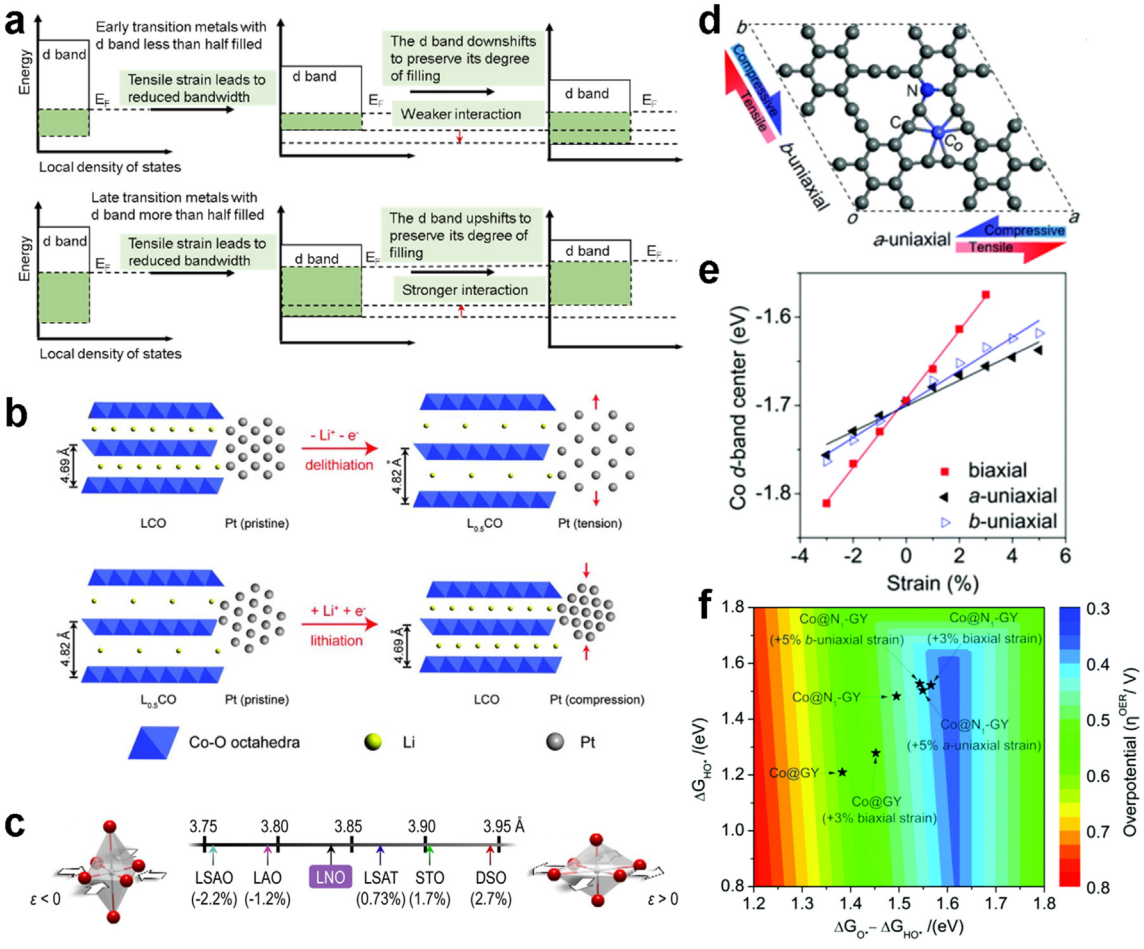

Fig. 8. (a) Energy diagrams explaining the influence of tensile strain on the position of the d-band for early transition metals and late transition metals. Reproduced with permission [143]. Copyright 2017, Springer Nature. (b) Schematic of the lattice constant change in $LiCoO_2$ substrates and how lattice strains are induced in Pt nanoparticles. Reproduced with permission [144]. Copyright 2016, American Association for the Advancement of Science. (c) Lattice parameters and associated biaxial strain for LNO on various substrates. Reproduced with permission [145]. Copyright 2016, American Chemical Society. (d) Structure of Co@N_1-GY. Biaxial strain means the simultaneous occurrence of both a and b uniaxial strains. Reproduced with permission [146]. Copyright 2020, Royal Society of Chemistry. (e) The d-band center of the Co atom as a function of lattice strain. Reproduced with permission [146]. (f) Colored counter plot representing an OER performance volcano. The units of the η_{OER} color bar values are V vs. RHE. Reproduced with permission [146].

compressive strain to tensile strain, reaching the lowest overpotential of 0.33 V with 3% biaxial tensile strain (Fig. 8f).

Additionally, strain induction was reported to tune the band structure of single-walled carbon nanotubes [147]. Theoretical studies predicted that band gap changes could range between ±100 meV per 1% stretch, according to carbon nanotube chirality, and this prediction agreed well with experimental measurements. For graphene, theoretical calculation revealed that a uniform uniaxial strain shifted the Dirac cones at K and K' points in opposite directions, thus inducing a pseudo-magnetic field and altering the electronic structure of graphene [148]. Additionally, the G band and 2D band of graphene in the Raman spectrum tended to split into two subpeaks by strain. Therefore, the introduction of strain in carbon-based materials can optimize the adsorption energy of O intermediates so as to increase the electrocatalytic performance. Moreover, early studies reported the introduction of heteroatoms or functional groups would generate strain in carbon materials [149]. For example, Huang et al. determined that the doping of large Se atoms into CNT-graphene caused high strain at the edge sites, which facilitated charge localization and promoted the associated chemisorption of oxygen [150]. As a result, Se-doped CNT-graphene exhibited good ORR activity, long stability, and high resistance to methanol compared with commercial Pt/C. This study suggested that developing carbon materials doped with Se or other large dopants offers a new strategy to induce strain and improve catalytic activity.

4.4. *Interface construction*

Interface refers to the boundary between two different phases. Interface engineering (e.g., physical stacking or chemical interfacial bonding) can induce intriguing physicochemical properties at the interface area and strong synergistic effects for oxygen electrocatalysis [151]. The synergistic effects include the following: 1) mismatched lattices induce structural disorder, defects, and multiple phases, providing rich active sites; 2) the interface offers desirable channels for charge and mass transport, enabling favorable contact between the electrolyte and the active sites; 3) a robust interface allows enhanced electronic conductivity and mechanical stability; 4) electron redistribution optimizes the adsorption/desorption of intermediates [152]. Various interfaces have been constructed with transition metal compounds, SACs, and metal-free materials.

Defects and structural disorder at the heterointerface of different transition metal compounds relieve induced strain and stabilize the interfacial structure. In addition, abundant unsaturated sites caused by the generated defects and structural mismatch can serve as atomic traps to enhance the adsorption ability of O intermediates, thus promoting catalytic activity. The significant effect of interface-induced defects in tuning catalytic activity has been extensively proven in previous studies [153]. For example, Chen and co-workers reported porous graphitized carbon-supported metallic Co and spinel oxide Co_3O_4 "Janus" nanoparticles (Co/Co_3O_4@PGS) for bifunctional oxygen catalysts (Fig. 9a) [154]. The defect-rich interface between Co and Co_3O_4 acted as an atomic trap that enabled exceptional O-intermediate adsorption capability. Consequently, Co/Co_3O_4@PGS displayed a high ORR $E_{1/2}$ of 0.89 V vs. RHE and a low OER $E_{j=10}$ of 1.58 V vs. RHE. Moreover, the constructed heterointerface was found to promote charge transfer, optimize electronic structure, and thus improve electrocatalytic activity. Recently, Kanatzidis et al. reported a nano-assembled hierarchical heterostructure consisting of Co_9S_8 and MoS_2 nanosheets on Ni_3S_2 nanorod arrays [155]. The assembled structure exhibited synergistic effects due to charge transfer through the constructed interfaces, delivering a high OER activity with an $E_{j=10}$ of 1.396 V.

Interface construction has also been applied between different SACs to yield improved ORR/OER performance. For example, Ma's group assembled Ni- and Fe-based SACs on the inner and outer surfaces of hollow graphene nanospheres, respectively (denoted as Ni–N_4/GHSs/Fe–N_4) [156]. Ni–N_4/GHSs/Fe–N_4 exhibited good bifunctional oxygen

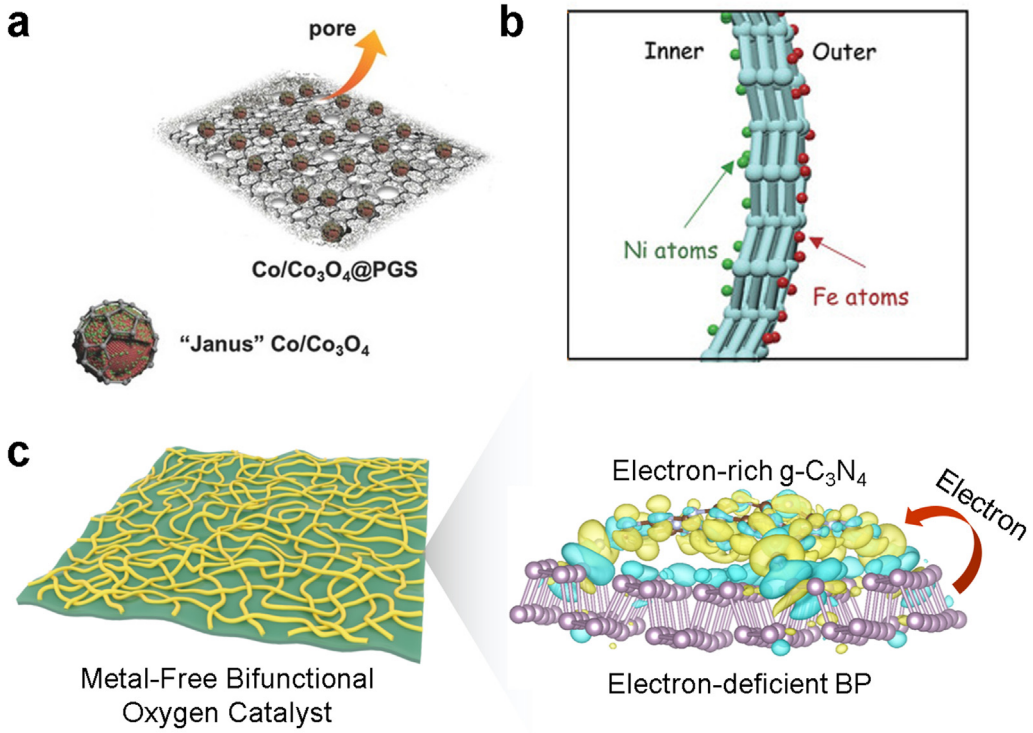

Fig. 9. (a) Illustration of Co and Co_3O_4 "Janus" nanoparticles. The red part represents metallic Co, and the green part represents Co_3O_4. Reproduced with permission [154]. Copyright 2018, Wiley-VCH. (b) Schematic of Janus Ni–N_4/GHSs/Fe–N_4 interfaces. Reproduced with permission [156]. Copyright 2020, Wiley-VCH. (c) Illustration of BP-CN-*c* heterostructure and the electron-density difference at the P–N bonded isosurfaces. The purple, brown, and light-blue spheres represent P, C, and N atoms, respectively. The yellow and cyan regions correspond to electron accumulation and depletion, respectively (isosurface of 0.00185 e $Å^{-3}$). Reproduced with permission [3]. Copyright 2021, Wiley-VCH.

activities due to the unique Janus-structured dual SACs architecture (Fig. 9b). In detail, the outer Fe-based SACs were responsible for the high ORR activity, while the inner Ni-based SACs predominantly contributed to the excellent activity towards the OER. As a result of the synergistic effect, Ni–N_4/GHSs/Fe–N_4 demonstrated high ORR activity, with an E_{onset} of 0.93 V, an $E_{1/2}$ of 0.83 V, and a small Tafel slope of 55 mV dec^{-1}, as well as good OER activity, with an $E_{j=10}$ of 1.62 V and a low Tafel slope of 81 mV dec^{-1}.

Based on the heterointerface construction strategy, our group recently developed an efficient metal-free bifunctional oxygen catalyst by covalently bonding 2D black phosphorus (BP) with g-C_3N_4 (denoted as BP-CN-*c*) [3]. The polarized P–N bond significantly directed the electron transfer at the BP/g-C_3N_4 interface, which produced electron-deficient BP planes and thus greatly promoted OOH* adsorption on P sites in the OER process (Fig. 9c). Moreover, BP-CN-*c* also delivered excellent ORR activity, which was attributed to electron-rich C sites at the interfaces and

Table 1
Performance of state-of-the-art ORR and OER catalysts.

Catalyst	Catalyst type	Regulation strategy	Electronic structure criteria	ORR performance (V vs. RHE)	OER performance (V vs. RHE)	Ref.
Co–NiO	Transition metal compounds	Heteroatom doping	Occupied electronic state at E_f	E_{onset} = 0.92; $E_{1/2}$ = 0.79	$E_{j=10}$ = 1.53	[101]
NiCo–FeO	Transition metal compounds	Heteroatom doping	Electronic states near the E_f	/	$E_{j=10}$ = 1.431; Tafel slope = 39 mV dec^{-1}	[102]
P–MoS_2	Transition metal compounds	Heteroatom doping	Oxygen-intermediate adsorption/ desorption change	E_{onset} and $E_{1/2}$ = 160 mV positive shift; 7-fold current density increase	/	[110]
Zn/CoN–C	SACs	Heteroatom doping	Enhanced binding ability of O_2	$E_{1/2}$ = 0.861	/	[113]
(Fe, Co) /CNT	SACs	Heteroatom doping	Activation of O_2	E_{onset} = 1.15; $E_{1/2}$ = 0.954	/	[114]
CoNi–SAs/NC	SACs	Heteroatom doping	Optimize O-intermediate adsorption/ desorption	E_{onset} = 0.88; $E_{1/2}$ = 0.76; J_k = 23.2 mA cm^{-2} at 0.5 V	/	[115]
FeNi SAs/NC	SACs	Heteroatom doping	Reduce the energy barrier of RDS	E_{onset} = 0.98; $E_{1/2}$ = 0.84	$E_{j=10}$ = 1.5; Tafel slope = 54.68 mV dec^{-1}	[116]
Zn,Co-Nx-C-Sy	SACs	Heteroatom doping	Charges around Zn,Co active centers; Facilitate O–O activation	$E_{1/2}$ = 0.893	/	[117]
Fe–SAs /NSC	SACs	Heteroatom doping	Increased electron density; High DOSs near the E_f	E_{onset} = 1.00; $E_{1/2}$ = 0.87	/	[121]
S|NiNx	SACs	Heteroatom doping	Improved local electronic states	/	$E_{j=10}$ = 1.51; Tafel slope = 45 mV dec^{-1}	[103]
Fe–N/P–C	SACs	Heteroatom doping	Favored oxygen intermediate adsorption/ desorption	E_{onset} = 0.941; $E_{1/2}$ = 0.867	$E_{j=10}$ = 1.61	[122]
Co–N,B-CSs	SACs	Heteroatom doping	Activate electron transfer; Strengthen interaction with the oxygen intermediate	$E_{1/2}$ = 0.83; limiting current density = 5.66 mA cm^{-2}	$E_{j=10}$ = 1.66	[104]
O–Zr–N–C	SACs	Heteroatom doping	d-band center	$E_{1/2}$ = 0.91	/	[105]
SC CoO NRs	Transition metal compounds	Vacancy creation	Induce new electronic states in the band gap	E_{onset} = 0.96; $E_{1/2}$ = 0.85	/	[129]
Co_3O_4	Transition metal compounds	Vacancy creation	Generation of new gap states	/	E_{onset} = 1.52	[125]
$La_{1-x}FeO_{3-\delta}$	Transition metal compounds	Vacancy creation	Optimal e_g orbital filling	$E_{1/2}$ = 0.6	E_{onset} = 1.64	[130]
Ultrathin $CoSe_2$	Transition metal compounds	Vacancy creation	Facilitate H_2O adsorption	/	$E_{j=10}$ = 1.55	[138]
Fe–N_x/C	SACs	Vacancy creation	Favorable O_2 adsorption energy	E_{onset} = 0.88	/	[139]
MgN_2C	SACs	Vacancy creation	Optimal adsorption for O intermediates	E_{onset} = 1.03; $E_{1/2}$ = 0.91; Tafel slope = 62 mV dec^{-1}	/	[131]
Fe/OES	SACs	Vacancy creation	Favorable ORR pathway	E_{onset} = 1.0; $E_{1/2}$ = 0.85	/	[140]
FeN_4-6r-c2	SACs	Vacancy creation	Decreased overall ORR barriers	$E_{1/2}$ = 0.95	/	[132]
Fe–N/S-CNT–GR	SACs	Vacancy creation	Favorable ORR pathway	$E_{1/2}$ = 0.91	$E_{j=10}$ = 1.6	[141]
NGM	Metal-free catalysts	Vacancy creation	Regulate the binding energy	E_{onset} = 0.89; $E_{1/2}$ = 0.77	$E_{j=10}$ = 1.67	[133]
$LaNiO_3$	Transition metal compounds	Strain induction	Weight the center of each orbital state to its orbital occupancy	0.823 V at overpotentials of η = 400 mV	1.623 V at overpotentials of η = 400 mV	[145]
Co@N_1-GY	SACs	Strain induction	d-band center	/	$E_{j=10}$ = 1.56	[146]
Co/Co_3O_4@PGS	Transition metal compounds	Interface construction	O intermediates adsorption	$E_{1/2}$ = 0.89	$E_{j=10}$ = 1.58	[154]
MoS_2/Co_9S_8/ Ni_3S_2/Ni	Transition metal compounds	Interface construction	Charge transfer	/	$E_{j=10}$ = 1.396	[155]
Ni–N_4/GHSs/ Fe–N_4	SACs	Interface construction	Synergistic effect between Ni and Fe	E_{onset} = 0.93; $E_{1/2}$ = 0.83; Tafel slope = 55 mV dec^{-1}	$E_{j=10}$ = 1.62; Tafel slope = 81 mV dec^{-1}	[156]
BP-CN-*c*	Metal-free catalysts	Interface construction	Electron transfer and OOH* adsorption promotion	$E_{1/2}$ = 0.84	$E_{j=10}$ = 1.58	[3]

reduced energy barriers for the RDS of ORR. Impressively, BP-CN-*c* yielded state-of-the-art OER performance, with an $E_{j=10}$ of 1.58 V and a good stability of 90% retention after 10 h of operation, compared to other reported BP-based metal-free catalysts. In addition, BP-CN-*c* exhibited a high ORR $E_{1/2}$ of 0.84 V, making it the first BP-based metal-free bifunctional oxygen catalyst.

Apart from heterostructures based on double transition metal compounds, double SACs, or double metal-free materials, interfaces have also been constructed between different types of catalysts to modify the electronic structure of various components and improve the oxygen electrocatalytic performance [152,157]. For example, Lou's group synthesized MnO/Co in porous graphitic carbon polyhedrons (MnO/-Co/PGC) with abundant heterointerfaces for both the ORR and the OER [158]. The OER activity was improved by increased conductivity deriving from well-defined heterointerfaces generated *in situ* via Co nanocrystals and the formation of robust graphitic carbon. Due to the constructed heterostructures, the assembled MnO/Co/PGC exhibited excellent activity and stability towards both the ORR (E_{onset} of 0.95 V vs. RHE, $E_{1/2}$ of 0.78 V vs. RHE, and limited current density of 6.0 mA cm^{-2}) and the OER ($E_{j=10}$ of 1.537 V vs. RHE and Tafel slope of 77 mV dec^{-1}).

5. Conclusions and outlook

Improving the sluggish kinetics of oxygen electrocatalysis remains a critical task for achieving enhanced energy conversion and storage efficiency. Studies on the regulation of electrocatalyst electronic structure, which is closely related to the adsorption of O intermediates, can provide important design criteria for tuning the intrinsic activity of oxygen catalysts. With the design principle established, one can bypass routine trial and error and accelerate the search process for high-performance catalysts. In this review article, we have summarized the strategies employed thus far to regulate the intrinsic activity of noble metal-free electrocatalysts for alkaline oxygen electrocatalysis, including diverse transition metal compounds, SACs, and metal-free catalysts (Table 1). We have also discussed the relationship between electronic structure and oxygen electrocatalytic activities. Despite the fact that substantial efforts have been made, some key obstacles remain and should be addressed by future efforts. Perspectives and challenges in these areas are discussed below.

1) **Controllable synthesis of catalysts with defined structures.** Precise quantification of heteroatom doping, vacancy creation, strain induction, or interface construction requires identifying with high accuracy the spatial positions of active sites in the catalyst. Catalysts with well-defined structures are expected to provide effective models to investigate structure–catalytic performance relationships, which would, in turn, support the design of advanced oxygen catalytic materials.
2) **Establishing universal and comprehensive principles for complex electronic structure regulation.** In realistic cases, electronic structural engineering strategies could trigger multiple effects. For example, both strain and defects can be identified when catalysts are promoted by constructing interfaces. It is therefore challenging to distinguish the contribution of an individual effect. Figuring out the exact origin of different effects is of great significance for rationally designing electrocatalysts in the future.
3) **Finding reliable electronic structure descriptors for catalytic properties.** The current descriptors, including e_g filling, d-band theory, oxygen p-band center, charge-transfer energy, Fermi softness, as well as the average O *2p* state energy, are not universal descriptors. For example, the popular d-band theory fails to explain the changes in adsorption strength and electrocatalytic activity induced by strain. This fact calls for the exploration of more accurate electronic structure descriptors for catalytic properties. To this end, it is essential to combine experimental and theoretical approaches to establish a universal relationship between electronic structure and electrocatalytic activity, which could in turn be used to direct new catalyst design.
4) **Building accurate theoretical models for the catalytic process.** Discrepancies between theoretical and realistic catalyst models should be taken seriously, in particular for catalysts that undergo surface reconstruction during the catalytic reactions. For example, transition metal compounds, like TMCs, TMPs, and TMNs, undergo surface reconstruction in the OER process. Likely, self-adjusting was previously observed for SACs during the catalytic process. Therefore, theoretical calculations should track the complete catalytic process and use rational modelling to demonstrate the evolution of active sites.
5) **Developing advanced characterization techniques.** Advanced characterization techniques, in particular atomic-resolution and *in situ* characterization methods, are still much needed to elucidate catalyst structure and catalytic mechanisms. Ideally, these characterization techniques provide direct evidence of active site structural evolution during practical reaction conditions, help to build accurate structural models for theoretical simulation, and provide strong evidence for understanding catalytic mechanisms. In this regard, the correlation between electronic structure and catalyst performance should be derived at a deep level to accelerate the rational development of new catalysts.
6) **Developing catalysts with long-term stability.** Compared with catalytic activity, the stability issue has often been overlooked. The application of electrocatalysts in various devices requires the development of long-term stable materials. For transition metal compounds, the doping strategy is generally applied to improve stability, especially under the harsh corrosion and high anodic potential of the OER. In the case of metal-free carbon-based catalysts, their stability can be enhanced by increasing the carbon graphitization degree. Moreover, it is necessary to establish a standard test protocol for assessing stability. The current lack of standardization for both testing and reporting catalyst stability makes it difficult to fairly compare results generated from different laboratories.

Author contributions

X. Wang conducted the literature search. All authors wrote, discussed, and revised the manuscript.

Declaration of competing interests

The authors declare that they have no known competing financial interests or personal relationships that could have appeared to influence the work reported in this paper.

Acknowledgments

This work was financially supported by European Union's Horizon 2020 research and innovation programme (GrapheneCore3 881603), Sächsisches Staatsministerium für Wissenschaft und Kunst (Sonderzuweisung zur Unterstützung profilbestimmender Struktureinheiten), German Research Foundation (DFG) within the Cluster of Excellence, and CRC 1415 (grant no. 417590517).

References

[1] Z.W. Seh, J. Kibsgaard, C.F. Dickens, I. Chorkendorff, J.K. Nørskov, T.F. Jaramillo, Combining theory and experiment in electrocatalysis: insights into materials design, Science 355 (2017) eaad4998.
[2] M.K. Debe, Electrocatalyst approaches and challenges for automotive fuel cells, Nature 486 (2012) 43–51.
[3] X. Wang, R.K.M. Raghupathy, C.J. Querebillo, Z. Liao, D. Li, K. Lin, M. Hantusch, Z. Sofer, B. Li, E. Zschech, Interfacial covalent bonds regulated electron-deficient 2D black phosphorus for electrocatalytic oxygen reactions, Adv. Mater. 33 (2021) 2008752.
[4] J.A. Zamora Zeledón, M.B. Stevens, G.K.K. Gunasooriya, A. Gallo, A.T. Landers, M.E. Kreider, C. Hahn, J.K. Nørskov, T.F. Jaramillo, Tuning the electronic structure of Ag-Pd alloys to enhance performance for alkaline oxygen reduction, Nat. Commun. 12 (2021) 620.

[5] T. Maiyalagan, K.A. Jarvis, S. Therese, P.J. Ferreira, A. Manthiram, Spinel-type lithium cobalt oxide as a bifunctional electrocatalyst for the oxygen evolution and oxygen reduction reactions, Nat. Commun. 5 (2014) 3949.
[6] Y. Yuan, J. Wang, S. Adimi, H. Shen, T. Thomas, R. Ma, J.P. Attfield, M. Yang, Zirconium nitride catalysts surpass platinum for oxygen reduction, Nat. Mater. 19 (2020) 282–286.
[7] E. Pomerantseva, F. Bonaccorso, X. Feng, Y. Cui, Y. Gogotsi, Energy storage: the future enabled by nanomaterials, Science 366 (2019) eaan8285.
[8] P. Sabatier, La catalyse en chimie organique, 1920.
[9] Y. Sun, S. Gao, F. Lei, Y. Xie, Atomically-thin two-dimensional sheets for understanding active sites in catalysis, Chem. Soc. Rev. 44 (2015) 623–636.
[10] J. Hwang, R.R. Rao, L. Giordano, Y. Katayama, Y. Yu, Y. Shao-Horn, Perovskites in catalysis and electrocatalysis, Science 358 (2017) 751–756.
[11] H. Yang, X. Han, A.I. Douka, L. Huang, L. Gong, C. Xia, H.S. Park, B.Y. Xia, Advanced oxygen electrocatalysis in energy conversion and storage, Adv. Funct. Mater. 31 (2021) 2007602.
[12] H.F. Wang, C. Tang, Q. Zhang, A review of precious-metal-free bifunctional oxygen electrocatalysts: rational design and applications in Zn−air batteries, Adv. Funct. Mater. 28 (2018) 1803329.
[13] J. Liu, H. Liu, H. Chen, X. Du, B. Zhang, Z. Hong, S. Sun, W. Wang, Progress and challenges toward the rational design of oxygen electrocatalysts based on a descriptor approach, Adv. Sci. 7 (2020) 1901614.
[14] Y. Wang, D. Wang, Y. Li, Rational design of single-atom site electrocatalysts: from theoretical understandings to practical applications, Adv. Mater. 33 (2021) 2008151.
[15] J.K. Nørskov, J. Rossmeisl, A. Logadottir, L. Lindqvist, J.R. Kitchin, T. Bligaard, H. Jonsson, Origin of the overpotential for oxygen reduction at a fuel-cell cathode, J. Phys. Chem. B 108 (2004) 17886–17892.
[16] J. Suntivich, H.A. Gasteiger, N. Yabuuchi, H. Nakanishi, J.B. Goodenough, Y. Shao-Horn, Design principles for oxygen-reduction activity on perovskite oxide catalysts for fuel cells and metal–air batteries, Nat. Chem. 3 (2011) 546–550.
[17] D. Guo, R. Shibuya, C. Akiba, S. Saji, T. Kondo, J. Nakamura, Active sites of nitrogen-doped carbon materials for oxygen reduction reaction clarified using model catalysts, Science 351 (2016) 361–365.
[18] F. Cheng, J. Chen, Metal–air batteries: from oxygen reduction electrochemistry to cathode catalysts, Chem. Soc. Rev. 41 (2012) 2172–2192.
[19] C. Zinola, A.J. Arvia, G. Estiu, E.A. Castro, A quantum chemical approach to the influence of platinum surface structure on the oxygen electroreduction reaction, J. Phys. Chem. 98 (1994) 7566–7576.
[20] C. Zhu, H. Li, S. Fu, D. Du, Y. Lin, Highly efficient nonprecious metal catalysts towards oxygen reduction reaction based on three-dimensional porous carbon nanostructures, Chem. Soc. Rev. 45 (2016) 517–531.
[21] Y. Nie, L. Li, Z. Wei, Recent advancements in Pt and Pt-free catalysts for oxygen reduction reaction, Chem. Soc. Rev. 44 (2015) 2168–2201.
[22] J. Rossmeisl, Z.-W. Qu, H. Zhu, G.-J. Kroes, J.K. Nørskov, Electrolysis of water on oxide surfaces, J. Electroanal. Chem. 607 (2007) 83–89.
[23] F. Calle-Vallejo, J.I. Martínez, J. Rossmeisl, Density functional studies of functionalized graphitic materials with late transition metals for oxygen reduction reactions, Phys. Chem. Chem. Phys. 13 (2011) 15639–15643.
[24] T. Tyson, Q. Qian, C.-C. Kao, J.-P. Rueff, F. De Groot, M. Croft, S.-W. Cheong, M. Greenblatt, M. Subramanian, Valence state of Mn in Ca-doped $LaMnO_3$ studied by high-resolution Mn K β emission spectroscopy, Phys. Rev. B 60 (1999) 4665.
[25] C. Ritter, M. Ibarra, J. De Teresa, P. Algarabel, C. Marquina, J. Blasco, J. Garcia, S. Oseroff, S. Cheong, Influence of oxygen content on the structural, magnetotransport, and magnetic properties of $LaMnO_{3+\delta}$, Phys. Rev. B 56 (1997) 8902.
[26] B. Hammer, J.K. Nørskov, Theoretical surface science and catalysis—calculations and concepts, in: Advances in Catalysis, Elsevier, 2000, pp. 71–129.
[27] J. Greeley, I. Stephens, A. Bondarenko, T.P. Johansson, H.A. Hansen, T. Jaramillo, J. Rossmeisl, I. Chorkendorff, J.K. Nørskov, Alloys of platinum and early transition metals as oxygen reduction electrocatalysts, Nat. Chem. 1 (2009) 552–556.
[28] X. Liu, L. Dai, Carbon-based metal-free catalysts, Nat. Rev. Mater. 1 (2016) 1–12.
[29] C. Tang, H.-F. Wang, Q. Zhang, Multiscale principles to boost reactivity in gas-involving energy electrocatalysis, Acc. Chem. Res. 51 (2018) 881–889.
[30] A. Grimaud, W.T. Hong, Y. Shao-Horn, J.-M. Tarascon, Anionic redox processes for electrochemical devices, Nat. Mater. 15 (2016) 121–126.
[31] I.C. Man, H.Y. Su, F. Calle-Vallejo, H.A. Hansen, J.I. Martínez, N.G. Inoglu, J. Kitchin, T.F. Jaramillo, J.K. Nørskov, J. Rossmeisl, Universality in oxygen evolution electrocatalysis on oxide surfaces, ChemCatChem 3 (2011) 1159–1165.
[32] J. Suntivich, K.J. May, H.A. Gasteiger, J.B. Goodenough, Y. Shao-Horn, A perovskite oxide optimized for oxygen evolution catalysis from molecular orbital principles, Science 334 (2011) 1383–1385.
[33] A. Grimaud, K.J. May, C.E. Carlton, Y.-L. Lee, M. Risch, W.T. Hong, J. Zhou, Y. Shao-Horn, Double perovskites as a family of highly active catalysts for oxygen evolution in alkaline solution, Nat. Commun. 4 (2013) 2439.
[34] J. Song, C. Wei, Z.-F. Huang, C. Liu, L. Zeng, X. Wang, Z.J. Xu, A review on fundamentals for designing oxygen evolution electrocatalysts, Chem. Soc. Rev. 49 (2020) 2196–2214.
[35] A. Grimaud, A. Demortiere, M. Saubanere, W. Dachraoui, M. Duchamp, M.-L. Doublet, J.-M. Tarascon, Activation of surface oxygen sites on an iridium-based model catalyst for the oxygen evolution reaction, Nat. Energy 2 (2016) 1–10.
[36] Y. Pan, X. Xu, Y. Zhong, L. Ge, Y. Chen, J.-P.M. Veder, D. Guan, R. O'Hayre, M. Li, G. Wang, Direct evidence of boosted oxygen evolution over perovskite by enhanced lattice oxygen participation, Nat. Commun. 11 (2002) 2002.
[37] P. Gao, M. Grätzel, M.K. Nazeeruddin, Organohalide lead perovskites for photovoltaic applications, Energy Environ. Sci. 7 (2014) 2448–2463.
[38] J. Xu, C. Chen, Z. Han, Y. Yang, J. Li, Q. Deng, Recent advances in oxygen electrocatalysts based on perovskite oxides, Nanomaterials 9 (2019) 1161.
[39] C. Wei, Z. Feng, G.G. Scherer, J. Barber, Y. Shao-Horn, Z.J. Xu, Cations in octahedral sites: a descriptor for oxygen electrocatalysis on transition-metal spinels, Adv. Mater. 29 (2017) 1606800.
[40] R.L. Doyle, I.J. Godwin, M.P. Brandon, M.E. Lyons, Redox and electrochemical water splitting catalytic properties of hydrated metal oxide modified electrodes, Phys. Chem. Chem. Phys. 15 (2013) 13737–13783.
[41] H. Bode, K. Dehmelt, J. Witte, Zur kenntnis der nickelhydroxidelektrode—I. Über das nickel (II)-hydroxidhydrat, Electrochim. Acta 11 (1966) 1079–1087.
[42] K.E. Sickafus, J.M. Wills, N.W. Grimes, Structure of spinel, J. Am. Ceram. Soc. 82 (1999) 3279–3292.
[43] C. Mu, J. Mao, J. Guo, Q. Guo, Z. Li, W. Qin, Z. Hu, K. Davey, T. Ling, S.Z. Qiao, Rational design of spinel cobalt vanadate oxide Co_2VO_4 for superior electrocatalysis, Adv. Mater. 32 (2020) 1907168.
[44] N.-T. Suen, S.-F. Hung, Q. Quan, N. Zhang, Y.-J. Xu, H.M. Chen, Electrocatalysis for the oxygen evolution reaction: recent development and future perspectives, Chem. Soc. Rev. 46 (2017) 337–365.
[45] X.-M. Liu, X. Cui, K. Dastafkan, H.-F. Wang, C. Tang, C. Zhao, A. Chen, C. He, M. Han, Q. Zhang, Recent advances in spinel-type electrocatalysts for bifunctional oxygen reduction and oxygen evolution reactions, J. Energy Chem. 53 (2021) 290–302.
[46] K.N. Dinh, Q. Liang, C.-F. Du, J. Zhao, A.I.Y. Tok, H. Mao, Q. Yan, Nanostructured metallic transition metal carbides, nitrides, phosphides, and borides for energy storage and conversion, Nano Today 25 (2019) 99–121.
[47] S. Dong, X. Chen, X. Zhang, G. Cui, Nanostructured transition metal nitrides for energy storage and fuel cells, Coord. Chem. Rev. 257 (2013) 1946–1956.
[48] J. Houston, G. Laramore, R.L. Park, Surface electronic properties of tungsten, tungsten carbide, and platinum, Science 185 (1974) 258–260.
[49] M. Naguib, M. Kurtoglu, V. Presser, J. Lu, J. Niu, M. Heon, L. Hultman, Y. Gogotsi, M.W. Barsoum, Two-dimensional nanocrystals produced by exfoliation of Ti_3AlC_2, Adv. Mater. 23 (2011) 4248–4253.
[50] M. Naguib, O. Mashtalir, J. Carle, V. Presser, J. Lu, L. Hultman, Y. Gogotsi, M.W. Barsoum, Two-dimensional transition metal carbides, ACS Nano 6 (2012) 1322–1331.
[51] B. Sun, Q. Lu, K. Chen, W. Zheng, Z. Liao, N. Lopatik, D. Li, M. Hantusch, S. Zhou, H.I. Wang, Redox-active metaphosphate-like terminals enable high-capacity MXene anodes for ultrafast Na-ion storage, Adv. Mater. (2022) 2108682.
[52] M. Naguib, V.N. Mochalin, M.W. Barsoum, Y. Gogotsi, 25th anniversary article: MXenes: a new family of two-dimensional materials, Adv. Mater. 26 (2014) 992–1005.
[53] V. Kamysbayev, A.S. Filatov, H. Hu, X. Rui, F. Lagunas, D. Wang, R.F. Klie, D.V. Talapin, Covalent surface modifications and superconductivity of two-dimensional metal carbide MXenes, Science 369 (2020) 979–983.
[54] B. Aronsson, Borides, Silicides and Phosphides, Methuen, 1965.
[55] S.T. Oyama, T. Gott, H. Zhao, Y.-K. Lee, Transition metal phosphide hydroprocessing catalysts: a review, Catal. Today 143 (2009) 94–107.
[56] Z. Pu, T. Liu, I.S. Amiinu, R. Cheng, P. Wang, C. Zhang, P. Ji, W. Hu, J. Liu, S. Mu, Transition-metal phosphides: activity origin, energy-related electrocatalysis applications, and synthetic strategies, Adv. Funct. Mater. 30 (2020) 2004009.
[57] B. Qiu, L. Cai, Y. Wang, Z. Lin, Y. Zuo, M. Wang, Y. Chai, Fabrication of nickel–cobalt bimetal phosphide nanocages for enhanced oxygen evolution catalysis, Adv. Funct. Mater. 28 (2018) 1706008.
[58] C.S. Lim, C.K. Chua, Z. Sofer, K. Klímová, C. Boothroyd, M. Pumera, Layered transition metal oxyhydroxides as tri-functional electrocatalysts, J. Mater. Chem. A 3 (2015) 11920–11929.
[59] D.S. Hall, D.J. Lockwood, C. Bock, B.R. MacDougall, Nickel hydroxides and related materials: a review of their structures, synthesis and properties, Proc. R. Soc. A: Math. Phys. Eng. Sci. 471 (2015) 20140792.
[60] L. Trotochaud, S.L. Young, J.K. Ranney, S.W. Boettcher, Nickel–iron oxyhydroxide oxygen-evolution electrocatalysts: the role of intentional and incidental iron incorporation, J. Am. Chem. Soc. 136 (2014) 6744–6753.
[61] F. Dionigi, Z. Zeng, I. Sinev, T. Merzdorf, S. Deshpande, M.B. Lopez, S. Kunze, I. Zegkinoglou, H. Sarodnik, D. Fan, In-situ structure and catalytic mechanism of NiFe and CoFe layered double hydroxides during oxygen evolution, Nat. Commun. 11 (2020) 2522.
[62] L. Huang, Y. Zou, D. Chen, S. Wang, Electronic structure regulation on layered double hydroxides for oxygen evolution reaction, Chin. J. Catal. 40 (2019) 1822–1840.
[63] B. Zhang, X. Zheng, O. Voznyy, R. Comin, M. Bajdich, M. García-Melchor, L. Han, J. Xu, M. Liu, L. Zheng, Homogeneously dispersed multimetal oxygen-evolving catalysts, Science 352 (2016) 333–337.
[64] B.Q. Li, S.Y. Zhang, C. Tang, X. Cui, Q. Zhang, Anionic regulated NiFe (oxy) sulfide electrocatalysts for water oxidation, Small 13 (2017) 1700610.
[65] Y. Wang, Y. Zhang, Z. Liu, C. Xie, S. Feng, D. Liu, M. Shao, S. Wang, Layered double hydroxide nanosheets with multiple vacancies obtained by dry exfoliation as highly efficient oxygen evolution electrocatalysts, Angew. Chem. Int. Ed. 56 (2017) 5867–5871.
[66] W. Zhu, L. Liu, Z. Yue, W. Zhang, X. Yue, J. Wang, S. Yu, L. Wang, J. Wang, Au promoted nickel–iron layered double hydroxide nanoarrays: a modular catalyst enabling high-performance oxygen evolution, ACS Appl. Mater. Interfaces 9 (2017) 19807–19814.
[67] S.M. Tan, C.K. Chua, D. Sedmidubský, Z. Sofer, M. Pumera, Electrochemistry of layered GaSe and GeS: applications to ORR, OER and HER, Phys. Chem. Chem. Phys. 18 (2016) 1699–1711.
[68] Y. Wang, X. Li, M. Zhang, Y. Zhou, D. Rao, C. Zhong, J. Zhang, X. Han, W. Hu, Y. Zhang, Lattice-strain engineering of homogeneous $NiS_{0.5}Se_{0.5}$ core–shell

nanostructure as a highly efficient and robust electrocatalyst for overall water splitting, Adv. Mater. 32 (2020) 2000231.
[69] J. Zhang, H. Yang, B. Liu, Coordination engineering of single-atom catalysts for the oxygen reduction reaction: a review, Adv. Energy Mater. 11 (2021) 2002473.
[70] C.X. Zhao, B.Q. Li, J.N. Liu, Q. Zhang, Intrinsic electrocatalytic activity regulation of M–N–C single-atom catalysts for the oxygen reduction reaction, Angew. Chem. Int. Ed. 60 (2021) 4448–4463.
[71] H. Xu, D. Cheng, D. Cao, X.C. Zeng, A universal principle for a rational design of single-atom electrocatalysts, Nat. Catal. 1 (2018) 339–348.
[72] H. Peng, F. Liu, X. Liu, S. Liao, C. You, X. Tian, H. Nan, F. Luo, H. Song, Z. Fu, Effect of transition metals on the structure and performance of the doped carbon catalysts derived from polyaniline and melamine for ORR application, ACS Catal. 4 (2014) 3797–3805.
[73] H. Fei, J. Dong, Y. Feng, C.S. Allen, C. Wan, B. Volosskiy, M. Li, Z. Zhao, Y. Wang, H. Sun, General synthesis and definitive structural identification of MN_4C_4 single-atom catalysts with tunable electrocatalytic activities, Nat. Catal. 1 (2018) 63–72.
[74] R. Gusmão, M. Veselý, Z.k. Sofer, Recent developments on the single atom supported at 2D materials beyond graphene as catalysts, ACS Catal. 10 (2020) 9634–9648.
[75] X. Fu, N. Li, B. Ren, G. Jiang, Y. Liu, F.M. Hassan, D. Su, J. Zhu, L. Yang, Z. Bai, Tailoring FeN4 sites with edge enrichment for boosted oxygen reduction performance in proton exchange membrane fuel cell, Adv. Energy Mater. 9 (2019) 1803737.
[76] Y. Zhu, J. Sokolowski, X. Song, Y. He, Y. Mei, G. Wu, Engineering local coordination environments of atomically dispersed and heteroatom-coordinated single metal site electrocatalysts for clean energy-conversion, Adv. Energy Mater. 10 (2020) 1902844.
[77] H.B. Yang, J. Miao, S.-F. Hung, J. Chen, H.B. Tao, X. Wang, L. Zhang, R. Chen, J. Gao, H.M. Chen, Identification of catalytic sites for oxygen reduction and oxygen evolution in N-doped graphene materials: development of highly efficient metal-free bifunctional electrocatalyst, Sci. Adv. 2 (2016) e1501122.
[78] J. Zhang, Z. Zhao, Z. Xia, L. Dai, A metal-free bifunctional electrocatalyst for oxygen reduction and oxygen evolution reactions, Nat. Nanotechnol. 10 (2015) 444–452.
[79] C. Tang, Q. Zhang, Nanocarbon for oxygen reduction electrocatalysis: dopants, edges, and defects, Adv. Mater. 29 (2017) 1604103.
[80] S. Zhao, D.W. Wang, R. Amal, L. Dai, Carbon-based metal-free catalysts for key reactions involved in energy conversion and storage, Adv. Mater. 31 (2019) 1801526.
[81] C. Hu, L. Dai, Carbon-based metal-free catalysts for electrocatalysis beyond the ORR, Angew. Chem. Int. Ed. 55 (2016) 11736–11758.
[82] X. Cai, L. Lai, J. Lin, Z. Shen, Recent advances in air electrodes for Zn–air batteries: electrocatalysis and structural design, Mater. Horiz. 4 (2017) 945–976.
[83] Y.J. Sa, C. Park, H.Y. Jeong, S.H. Park, Z. Lee, K.T. Kim, G.G. Park, S.H. Joo, Carbon nanotubes/heteroatom-doped carbon core–sheath nanostructures as highly active, metal-free oxygen reduction electrocatalysts for alkaline fuel cells, Angew. Chem. Int. Ed. 126 (2014) 4186–4190.
[84] D.S. Su, S. Perathoner, G. Centi, Nanocarbons for the development of advanced catalysts, Chem. Rev. 113 (2013) 5782–5816.
[85] G.L. Tian, Q. Zhang, B. Zhang, Y.G. Jin, J.Q. Huang, D.S. Su, F. Wei, Toward full exposure of "active sites": nanocarbon electrocatalyst with surface enriched nitrogen for superior oxygen reduction and evolution reactivity, Adv. Funct. Mater. 24 (2014) 5956–5961.
[86] T.V. Tam, S.G. Kang, M.H. Kim, S.G. Lee, S.H. Hur, J.S. Chung, W.M. Choi, Novel graphene hydrogel/B-doped graphene quantum dots composites as trifunctional electrocatalysts for Zn−air batteries and overall water splitting, Adv. Energy Mater. 9 (2019) 1900945.
[87] Z.W. Liu, F. Peng, H.J. Wang, H. Yu, W.X. Zheng, J. Yang, Phosphorus-doped graphite layers with high electrocatalytic activity for the O_2 reduction in an alkaline medium, Angew. Chem. Int. Ed. 50 (2011) 3257–3261.
[88] W. Lei, Y.-P. Deng, G. Li, Z.P. Cano, X. Wang, D. Luo, Y. Liu, D. Wang, Z. Chen, Two-dimensional phosphorus-doped carbon nanosheets with tunable porosity for oxygen reactions in zinc-air batteries, ACS Catal. 8 (2018) 2464–2472.
[89] I.Y. Jeon, S. Zhang, L. Zhang, H.J. Choi, J.M. Seo, Z. Xia, L. Dai, J.B. Baek, Edge-selectively sulfurized graphene nanoplatelets as efficient metal-free electrocatalysts for oxygen reduction reaction: the electron spin effect, Adv. Mater. 25 (2013) 6138–6145.
[90] J.P. Paraknowitsch, A. Thomas, Doping carbons beyond nitrogen: an overview of advanced heteroatom doped carbons with boron, sulphur and phosphorus for energy applications, Energy Environ. Sci. 6 (2013) 2839–2855.
[91] Y.P. Zhu, C. Guo, Y. Zheng, S.-Z. Qiao, Surface and interface engineering of noble-metal-free electrocatalysts for efficient energy conversion processes, Acc. Chem. Res. 50 (2017) 915–923.
[92] H. Cui, Z. Zhou, D. Jia, Heteroatom-doped graphene as electrocatalysts for air cathodes, Mater. Horiz. 4 (2017) 7–19.
[93] G.-L. Chai, K. Qiu, M. Qiao, M.-M. Titirici, C. Shang, Z. Guo, Active sites engineering leads to exceptional ORR and OER bifunctionality in P, N Co-doped graphene frameworks, Energy Environ. Sci. 10 (2017) 1186–1195.
[94] A. Shen, Y. Zou, Q. Wang, R.A. Dryfe, X. Huang, S. Dou, L. Dai, S. Wang, Oxygen reduction reaction in a droplet on graphite: direct evidence that the edge is more active than the basal plane, Angew. Chem. Int. Ed. 126 (2014) 10980–10984.
[95] H.-F. Wang, C. Tang, B. Wang, B.-Q. Li, X. Cui, Q. Zhang, Defect-rich carbon fiber electrocatalysts with porous graphene skin for flexible solid-state zinc–air batteries, Energy Stor. Mater. 15 (2018) 124–130.
[96] Z. Liu, Z. Zhao, Y. Wang, S. Dou, D. Yan, D. Liu, Z. Xia, S. Wang, In situ exfoliated, edge-rich, oxygen-functionalized graphene from carbon fibers for oxygen electrocatalysis, Adv. Mater. 29 (2017) 1606207.
[97] Z. Lu, J. Wang, S. Huang, Y. Hou, Y. Li, Y. Zhao, S. Mu, J. Zhang, Y. Zhao, N, B-codoped defect-rich graphitic carbon nanocages as high performance multifunctional electrocatalysts, Nano Energy 42 (2017) 334–340.
[98] Y. Yin, J. Han, Y. Zhang, X. Zhang, P. Xu, Q. Yuan, L. Samad, X. Wang, Y. Wang, Z. Zhang, Contributions of phase, sulfur vacancies, and edges to the hydrogen evolution reaction catalytic activity of porous molybdenum disulfide nanosheets, J. Am. Chem. Soc. 138 (2016) 7965–7972.
[99] A. Zhang, Y. Liang, H. Zhang, Z. Geng, J. Zeng, Doping regulation in transition metal compounds for electrocatalysis, Chem. Soc. Rev. 50 (2021) 9817–9844.
[100] L. Zhu, D. Zheng, Z. Wang, X. Zheng, P. Fang, J. Zhu, M. Yu, Y. Tong, X. Lu, A confinement strategy for stabilizing ZIF-derived bifunctional catalysts as a benchmark cathode of flexible all-solid-state zinc–air batteries, Adv. Mater. 30 (2018) 1805268.
[101] J. Qian, X. Guo, T. Wang, P. Liu, H. Zhang, D. Gao, Bifunctional porous Co-doped NiO nanoflowers electrocatalysts for rechargeable zinc-air batteries, Appl. Catal. B 250 (2019) 71–77.
[102] Y. Liu, Y. Ying, L. Fei, Y. Liu, Q. Hu, G. Zhang, S.Y. Pang, W. Lu, C.L. Mak, X. Luo, Valence engineering via selective atomic substitution on tetrahedral sites in spinel oxide for highly enhanced oxygen evolution catalysis, J. Am. Chem. Soc. 141 (2019) 8136–8145.
[103] Y. Hou, M. Qiu, M.G. Kim, P. Liu, G. Nam, T. Zhang, X. Zhuang, B. Yang, J. Cho, M. Chen, Atomically dispersed nickel–nitrogen–sulfur species anchored on porous carbon nanosheets for efficient water oxidation, Nat. Commun. 10 (2019) 1392.
[104] Y. Guo, P. Yuan, J. Zhang, Y. Hu, I.S. Amiinu, X. Wang, J. Zhou, H. Xia, Z. Song, Q. Xu, Carbon nanosheets containing discrete Co-N x-B y-C active sites for efficient oxygen electrocatalysis and rechargeable Zn–Air Batteries, ACS Nano 12 (2018) 1894–1901.
[105] X. Wang, Y. An, L. Liu, L. Fang, Y. Liu, J. Zhang, H. Qi, T. Heine, T. Li, A. Kuc, Atomically dispersed pentacoordinated-zirconium catalyst with axial oxygen ligand for oxygen reduction reaction, Angew. Chem. Int. Ed. 134 (2022) e202209746.
[106] Z. Zhao, M. Li, L. Zhang, L. Dai, Z. Xia, Design principles for heteroatom-doped carbon nanomaterials as highly efficient catalysts for fuel cells and metal–air batteries, Adv. Mater. 27 (2015) 6834–6840.
[107] L. Guo, J. Deng, G. Wang, Y. Hao, K. Bi, X. Wang, Y. Yang, N, P-doped CoS2 embedded in TiO_2 Nanoporous films for Zn–air batteries, Adv. Funct. Mater. 28 (2018) 1804540.
[108] Z. Wang, W. Xu, X. Chen, Y. Peng, Y. Song, C. Lv, H. Liu, J. Sun, D. Yuan, X. Li, Defect-rich nitrogen doped Co_3O_4/C porous nanocubes enable high-efficiency bifunctional oxygen electrocatalysis, Adv. Funct. Mater. 29 (2019) 1902875.
[109] M. Yu, Z. Wang, C. Hou, Z. Wang, C. Liang, C. Zhao, Y. Tong, X. Lu, S. Yang, Nitrogen-doped Co3O4 mesoporous nanowire arrays as an additive-free air-cathode for flexible solid-state zinc–air batteries, Adv. Mater. 29 (2017) 1602868.
[110] H. Huang, X. Feng, C. Du, W. Song, High-quality phosphorus-doped MoS_2 ultrathin nanosheets with amenable ORR catalytic activity, Chem. Commun. 51 (2015) 7903–7906.
[111] T. Sun, S. Mitchell, J. Li, P. Lyu, X. Wu, J. Pérez-Ramírez, J. Lu, Design of local atomic environments in single-atom electrocatalysts for renewable energy conversions, Adv. Mater. 33 (2021) 2003075.
[112] Y. Zhu, J. Sokolowski, X. Song, Y. He, Y. Mei, G. Wu, Single-atom catalysts: engineering local coordination environments of atomically dispersed and heteroatom-coordinated single metal site electrocatalysts for clean energy-conversion, Adv. Energy Mater. 10 (2020) 2070051.
[113] Z. Lu, B. Wang, Y. Hu, W. Liu, Y. Zhao, R. Yang, Z. Li, J. Luo, B. Chi, Z. Jiang, An isolated zinc–cobalt atomic pair for highly active and durable oxygen reduction, Angew. Chem. Int. Ed. 131 (2019) 2648–2652.
[114] J. Wang, W. Liu, G. Luo, Z. Li, C. Zhao, H. Zhang, M. Zhu, Q. Xu, X. Wang, C. Zhao, Synergistic effect of well-defined dual sites boosting the oxygen reduction reaction, Energy Environ. Sci. 11 (2018) 3375–3379.
[115] X. Han, X. Ling, D. Yu, D. Xie, L. Li, S. Peng, C. Zhong, N. Zhao, Y. Deng, W. Hu, Atomically dispersed binary Co-Ni sites in nitrogen-doped hollow carbon nanocubes for reversible oxygen reduction and evolution, Adv. Mater. 31 (2019) 1905622.
[116] D. Yu, Y. Ma, F. Hu, C.C. Lin, L. Li, H.Y. Chen, X. Han, S. Peng, Dual-sites coordination engineering of single atom catalysts for flexible metal–air batteries, Adv. Energy Mater. 11 (2021) 2101242.
[117] D. Liu, B. Wang, H. Li, S. Huang, M. Liu, J. Wang, Q. Wang, J. Zhang, Y. Zhao, Distinguished Zn, Co-Nx-C-Sy active sites confined in dentric carbon for highly efficient oxygen reduction reaction and flexible Zn-air batteries, Nano Energy 58 (2019) 277–283.
[118] H. Shang, X. Zhou, J. Dong, A. Li, X. Zhao, Q. Liu, Y. Lin, J. Pei, Z. Li, Z. Jiang, Engineering unsymmetrically coordinated $Cu\text{-}S_1N_3$ single atom sites with enhanced oxygen reduction activity, Nat. Commun. 11 (2020) 3049.
[119] P. Chen, N. Zhang, T. Zhou, Y. Tong, W. Yan, W. Chu, C. Wu, Y. Xie, Tailoring electronic structure of atomically dispersed metal–N3S1 active sites for highly efficient oxygen reduction catalysis, ACS Mater. Lett. 1 (2019) 139–146.
[120] C. Tang, Y. Jiao, B. Shi, J.N. Liu, Z. Xie, X. Chen, Q. Zhang, S.Z. Qiao, Coordination tunes selectivity: two-electron oxygen reduction on high-loading molybdenum single-atom catalysts, Angew. Chem. Int. Ed. 132 (2020) 9256–9261.
[121] J. Zhang, Y. Zhao, C. Chen, Y.-C. Huang, C.-L. Dong, C.-J. Chen, R.-S. Liu, C. Wang, K. Yan, Y. Li, Tuning the coordination environment in single-atom catalysts to achieve highly efficient oxygen reduction reactions, J. Am. Chem. Soc. 141 (2019) 20118–20126.

[122] K. Yuan, D. Lützenkirchen-Hecht, L. Li, L. Shuai, Y. Li, R. Cao, M. Qiu, X. Zhuang, M.K. Leung, Y. Chen, Boosting oxygen reduction of single iron active sites via geometric and electronic engineering: nitrogen and phosphorus dual coordination, J. Am. Chem. Soc. 142 (2020) 2404–2412.
[123] E. Jung, H. Shin, B.-H. Lee, V. Efremov, S. Lee, H.S. Lee, J. Kim, W. Hooch Antink, S. Park, K.-S. Lee, Atomic-level tuning of Co–N–C catalyst for high-performance electrochemical H_2O_2 production, Nat. Mater. 19 (2020) 436–442.
[124] J. Duan, S. Chen, C.A. Ortíz-Ledón, M. Jaroniec, S.Z. Qiao, Phosphorus vacancies that boost electrocatalytic hydrogen evolution by two orders of magnitude, Angew. Chem. Int. Ed. 59 (2020) 8181–8186.
[125] Y. Wang, T. Zhou, K. Jiang, P. Da, Z. Peng, J. Tang, B. Kong, W.B. Cai, Z. Yang, G. Zheng, Reduced mesoporous Co_3O_4 nanowires as efficient water oxidation electrocatalysts and supercapacitor electrodes, Adv. Energy Mater. 4 (2014) 1400696.
[126] M. Kuang, P. Han, L. Huang, N. Cao, L. Qian, G. Zheng, Electronic tuning of Co, Ni-based nanostructured (Hydr) oxides for aqueous electrocatalysis, Adv. Funct. Mater. 28 (2018) 1804886.
[127] L. Zhuang, L. Ge, Y. Yang, M. Li, Y. Jia, X. Yao, Z. Zhu, Ultrathin iron-cobalt oxide nanosheets with abundant oxygen vacancies for the oxygen evolution reaction, Adv. Mater. 29 (2017) 1606793.
[128] L. Xu, Q. Jiang, Z. Xiao, X. Li, J. Huo, S. Wang, L. Dai, Plasma-engraved Co_3O_4 nanosheets with oxygen vacancies and high surface area for the oxygen evolution reaction, Angew. Chem. Int. Ed. 128 (2016) 5363–5367.
[129] T. Ling, D.-Y. Yan, Y. Jiao, H. Wang, Y. Zheng, X. Zheng, J. Mao, X.-W. Du, Z. Hu, M. Jaroniec, Engineering surface atomic structure of single-crystal cobalt (II) oxide nanorods for superior electrocatalysis, Nat. Commun. 7 (2016) 12876.
[130] Y. Zhu, W. Zhou, J. Yu, Y. Chen, M. Liu, Z. Shao, Enhancing electrocatalytic activity of perovskite oxides by tuning cation deficiency for oxygen reduction and evolution reactions, Chem. Mater. 28 (2016) 1691–1697.
[131] S. Liu, Z. Li, C. Wang, W. Tao, M. Huang, M. Zuo, Y. Yang, K. Yang, L. Zhang, S. Chen, Turning main-group element magnesium into a highly active electrocatalyst for oxygen reduction reaction, Nat. Commun. 11 (2020) 938.
[132] R. Jiang, L. Li, T. Sheng, G. Hu, Y. Chen, L. Wang, Edge-site engineering of atomically dispersed Fe–N_4 by selective C–N bond cleavage for enhanced oxygen reduction reaction activities, J. Am. Chem. Soc. 140 (2018) 11594–11598.
[133] C. Tang, H.F. Wang, X. Chen, B.Q. Li, T.Z. Hou, B. Zhang, Q. Zhang, M.M. Titirici, F. Wei, Topological defects in metal-free nanocarbon for oxygen electrocatalysis, Adv. Mater. 28 (2016) 6845–6851.
[134] H.B. Tao, L. Fang, J. Chen, H.B. Yang, J. Gao, J. Miao, S. Chen, B. Liu, Identification of surface reactivity descriptor for transition metal oxides in oxygen evolution reaction, J. Am. Chem. Soc. 138 (2016) 9978–9985.
[135] Z. Hu, Z. Wu, C. Han, J. He, Z. Ni, W. Chen, Two-dimensional transition metal dichalcogenides: interface and defect engineering, Chem. Soc. Rev. 47 (2018) 3100–3128.
[136] C.R. Zhu, D. Gao, J. Ding, D. Chao, J. Wang, TMD-based highly efficient electrocatalysts developed by combined computational and experimental approaches, Chem. Soc. Rev. 47 (2018) 4332–4356.
[137] C. Das, N. Sinha, P. Roy, Transition metal non-oxides as electrocatalysts: advantages and challenges, Small 18 (2022) 2202033.
[138] Y. Liu, H. Cheng, M. Lyu, S. Fan, Q. Liu, W. Zhang, Y. Zhi, C. Wang, C. Xiao, S. Wei, Low overpotential in vacancy-rich ultrathin $CoSe_2$ nanosheets for water oxidation, J. Am. Chem. Soc. 136 (2014) 15670–15675.
[139] P. Song, Y. Wang, J. Pan, W. Xu, L. Zhuang, Structure-activity relationship in high-performance iron-based electrocatalysts for oxygen reduction reaction, J. Power Sources 300 (2015) 279–284.
[140] C.C. Hou, L. Zou, L. Sun, K. Zhang, Z. Liu, Y. Li, C. Li, R. Zou, J. Yu, Q. Xu, Single-atom iron catalysts on overhang-eave carbon cages for high-performance oxygen reduction reaction, Angew. Chem. Int. Ed. 132 (2020) 7454–7459.
[141] W.Y. Noh, J. Mun, Y. Lee, E.M. Kim, Y.K. Kim, K.Y. Kim, H.Y. Jeong, J.H. Lee, H.-K. Song, G. Lee, Molecularly engineered carbon platform to anchor edge-hosted single-atomic M–N/C (M= Fe, Co, Ni, Cu) electrocatalysts of outstanding durability, ACS Catal. 12 (2022) 7994–8006.
[142] T. Sun, J. Wang, C. Qiu, X. Ling, B. Tian, W. Chen, C. Su, B, N codoped and defect-rich nanocarbon material as a metal-free bifunctional electrocatalyst for oxygen reduction and evolution reactions, Adv. Sci. 5 (2018) 1800036.
[143] M. Luo, S. Guo, Strain-controlled electrocatalysis on multimetallic nanomaterials, Nat. Rev. Mater. 2 (2017) 1–13.
[144] H. Wang, S. Xu, C. Tsai, Y. Li, C. Liu, J. Zhao, Y. Liu, H. Yuan, F. Abild-Pedersen, F.B. Prinz, Direct and continuous strain control of catalysts with tunable battery electrode materials, Science 354 (2016) 1031–1036.
[145] J.R. Petrie, V.R. Cooper, J.W. Freeland, T.L. Meyer, Z. Zhang, D.A. Lutterman, H.N. Lee, Enhanced bifunctional oxygen catalysis in strained $LaNiO_3$ perovskites, J. Am. Chem. Soc. 138 (2016) 2488–2491.
[146] X. Gao, Y. Zhou, Y. Tan, S. Liu, Z. Cheng, Z. Shen, Strain effects on Co, N co-decorated graphyne catalysts for overall water splitting electrocatalysis, Phys. Chem. Chem. Phys. 22 (2020) 2457–2465.
[147] E. Minot, Y. Yaish, V. Sazonova, J.-Y. Park, M. Brink, P.L. McEuen, Tuning carbon nanotube band gaps with strain, Phys. Rev. Lett. 90 (2003) 156401.
[148] N. Levy, S. Burke, K. Meaker, M. Panlasigui, A. Zettl, F. Guinea, A.C. Neto, M.F. Crommie, Strain-induced pseudo–magnetic fields greater than 300 tesla in graphene nanobubbles, Science 329 (2010) 544–547.
[149] X. Xu, T. Liang, D. Kong, B. Wang, L. Zhi, Strain engineering of two-dimensional materials for advanced electrocatalysts, Mater, Today Nano 14 (2021) 100111.
[150] Z. Jin, H. Nie, Z. Yang, J. Zhang, Z. Liu, X. Xu, S. Huang, Metal-free selenium doped carbon nanotube/graphene networks as a synergistically improved cathode catalyst for oxygen reduction reaction, Nanoscale 4 (2012) 6455–6460.
[151] K. Novoselov, o.A. Mishchenko, o.A. Carvalho, A.C. Neto, 2D materials and van der Waals heterostructures, Science 353 (2016) aac9439.
[152] R. Zhao, Q. Li, X. Jiang, S. Huang, G. Fu, J.-M. Lee, Interface engineering in transition metal-based heterostructures for oxygen electrocatalysis, Mater. Chem. Front. 5 (2021) 1033–1059.
[153] J. Yin, Y. Li, F. Lv, Q. Fan, Y.-Q. Zhao, Q. Zhang, W. Wang, F. Cheng, P. Xi, S. Guo, NiO/CoN porous nanowires as efficient bifunctional catalysts for Zn–air batteries, ACS Nano 11 (2017) 2275–2283.
[154] Y. Jiang, Y.P. Deng, J. Fu, D.U. Lee, R. Liang, Z.P. Cano, Y. Liu, Z. Bai, S. Hwang, L. Yang, Interpenetrating triphase cobalt-based nanocomposites as efficient bifunctional oxygen electrocatalysts for long-lasting rechargeable zn–air batteries, Adv. Energy Mater. 8 (2018) 1702900.
[155] Y. Yang, H. Yao, Z. Yu, S.M. Islam, H. He, M. Yuan, Y. Yue, K. Xu, W. Hao, G. Sun, Hierarchical nanoassembly of MoS2/Co9S8/Ni3S2/Ni as a highly efficient electrocatalyst for overall water splitting in a wide pH range, J. Am. Chem. Soc. 141 (2019) 10417–10430.
[156] J. Chen, H. Li, C. Fan, Q. Meng, Y. Tang, X. Qiu, G. Fu, T. Ma, Dual single-atomic Ni-N4 and Fe-N4 sites constructing Janus hollow graphene for selective oxygen electrocatalysis, Adv. Mater. 32 (2020) 2003134.
[157] Q. Shao, P. Wang, X. Huang, Opportunities and challenges of interface engineering in bimetallic nanostructure for enhanced electrocatalysis, Adv. Funct. Mater. 29 (2019) 1806419.
[158] X.F. Lu, Y. Chen, S. Wang, S. Gao, X.W. Lou, Interfacing manganese oxide and cobalt in porous graphitic carbon polyhedrons boosts oxygen electrocatalysis for Zn–air batteries, Adv. Mater. 31 (2019) 1902339.